Design and formulation of functional pluripotent stem cell-derived cardiac microtissues

Nimalan Thavandiran[a,b], Nicole Dubois[c], Alexander Mikryukov[c], Stéphane Massé[d], Bogdan Beca[a,e], Craig A. Simmons[a,e], Vikram S. Deshpande[f], J. Patrick McGarry[g], Christopher S. Chen[h], Kumaraswamy Nanthakumar[d], Gordon M. Keller[c], Milica Radisic[a,b,i,1], and Peter W. Zandstra[a,b,c,i,j,1]

[a]Institute for Biomaterials and Biomedical Engineering, University of Toronto, Toronto, ON, Canada M5S 3G9; [b]Department of Chemical Engineering and Applied Chemistry, University of Toronto, Toronto, ON, Canada M5S 3E5; [d]Toby Hull Cardiac Fibrillation Management Laboratory, University of Toronto, Toronto, ON, Canada M5G 2C4; [e]Department of Mechanical and Industrial Engineering, University of Toronto, Toronto, ON, Canada M5S 3G8; [i]Heart & Stroke/Richard Lewar Centre of Excellence in Cardiovascular Research, University of Toronto, Toronto, ON, Canada M5S 3G2; and [j]Terrence Donnelly Centre for Cellular and Biomolecular Research, University of Toronto, Toronto, ON, Canada M5S 3E1; [c]McEwen Centre for Regenerative Medicine, University Health Network, Toronto, ON, Canada; [f]Department of Engineering, University of Cambridge, Cambridge, United Kingdom; [g]Mechanical and Biomedical Engineering, College of Engineering and Informatics, National University of Ireland, Galway, Ireland; and [h]Department of Bioengineering, University of Pennsylvania, Philadelphia, PA 19104

Edited by Shu Chien, University of California, San Diego, La Jolla, CA, and approved October 30, 2013 (received for review June 11, 2013)

Access to robust and information-rich human cardiac tissue models would accelerate drug-based strategies for treating heart disease. Despite significant effort, the generation of high-fidelity adult-like human cardiac tissue analogs remains challenging. We used computational modeling of tissue contraction and assembly mechanics in conjunction with microfabricated constraints to guide the design of aligned and functional 3D human pluripotent stem cell (hPSC)-derived cardiac microtissues that we term cardiac microwires (CMWs). Miniaturization of the platform circumvented the need for tissue vascularization and enabled higher-throughput image-based analysis of CMW drug responsiveness. CMW tissue properties could be tuned using electromechanical stimuli and cell composition. Specifically, controlling self-assembly of 3D tissues in aligned collagen, and pacing with point stimulation electrodes, were found to promote cardiac maturation-associated gene expression and in vivo-like electrical signal propagation. Furthermore, screening a range of hPSC-derived cardiac cell ratios identified that 75% NKX2 Homeobox 5 (NKX2-5)+ cardiomyocytes and 25% Cluster of Differentiation 90 OR (CD90)+ nonmyocytes optimized tissue remodeling dynamics and yielded enhanced structural and functional properties. Finally, we demonstrate the utility of the optimized platform in a tachycardic model of arrhythmogenesis, an aspect of cardiac electrophysiology not previously recapitulated in 3D in vitro hPSC-derived cardiac microtissue models. The design criteria identified with our CMW platform should accelerate the development of predictive in vitro assays of human heart tissue function.

microfabrication | heart regeneration | tissue engineering | cardiac toxicity | arrhythmia disease model

Directed differentiation strategies for generating and preserving human pluripotent stem cell (hPSC)-derived cardiomyocytes (CMs) are well-developed (1–7), and several CM cell-surface markers that can be used to enrich target subpopulations have been discovered (8, 9). Although differentiation of hPSCs into contracting CMs is well-established, their maturation into adult-equivalent cells, and their formulation into functional adult-like tissue, remains an unmet challenge (5). We and others have previously developed in vitro heart tissue models (10–12); however, these recently developed systems require further definition in terms of their underlying design criteria and the impact of key design parameters such as tissue geometry and input-cell composition on microtissue properties.

In the developing heart, gradients of cytokines drive differentiation along various cardiovascular lineages and, later, the adult heart is capable of dynamically maintaining a balanced composition of cardiomyocytes, cardiac fibroblasts, smooth muscle cells, and endothelial cells within a highly ordered extracellular matrix (ECM). It is through complex cell–cell and cell–ECM interactions that the heart maintains homeostasis and, to a limited extent, repair in response to ischemic injury (13). In contrast with this native microenvironment, conventional in vitro model platforms for drug screening and toxicity testing use tissue culture-treated polystyrene surfaces coated with a basal membrane. These 2D substrates lack topographical cues, limit cell–ECM adhesion to only one side of the cell, and have an elastic modulus that is orders of magnitude greater than the native substrate of the targeted cell type. Additionally, cardiomyocytes in these assays are cultured either on their own, with conditioned media from stromal cells, or with a physiologically inappropriate proportion of supporting cell types. It is established that multiple cell types are required to build physiological tissue (14). Supporting cells, such as cardiac fibroblasts, provide mechanotransductive cues and paracrine factors that influence cardiomyocyte assembly and maturation. In addition, gradients of electrical (15) and dynamic mechanical forces (16) provide critical electro- and mechanotransduction signaling throughout development and maturation (17) and following disease, injury, and repair. Cell morphology (18), rate of proliferation, migration (19), differentiation potential (20), drug responsiveness (12), and juxtracrine signaling (21) are all influenced by ECM-mediated mechanotransduction. To accurately determine the

Significance

Robust and predictive in vitro models of human cardiac tissue function could have transformative impact on our ability to test new drugs and understand cardiac disease. Despite significant effort, the generation of high-fidelity adult-like human cardiac tissue analogs remains challenging. In this paper, we systematically explore the design criteria for pluripotent stem cell-derived engineered cardiac tissue. Parameters such as biomechanical stress during tissue remodeling, input-cell composition, electrical stimulation, and tissue geometry are evaluated. Our results suggest that a specified combination of a 3D matrix-based microenvironment, uniaxial mechanical stress, and mixtures of cardiomyocytes and fibroblasts improves the performance and maturation state of in vitro engineered cardiac tissue.

Author contributions: N.T., N.D., A.M., C.S.C., G.M.K., M.R., and P.W.Z. designed research; N.T., N.D., A.M., S.M., V.S.D., and J.P.M. performed research; S.M., B.B., C.A.S., V.S.D., J.P.M., K.N., G.M.K., M.R., and P.W.Z. contributed new reagents/analytic tools; N.T., V.S.D., J.P.M., C.S.C., K.N., M.R., and P.W.Z. analyzed data; and N.T., M.R., and P.W.Z. wrote the paper.

The authors declare no conflict of interest.

This article is a PNAS Direct Submission.

Freely available online through the PNAS open access option.

[1]To whom correspondence may be addressed. E-mail: m.radisic@utoronto.ca or peter.zandstra@utoronto.ca.

This article contains supporting information online at www.pnas.org/lookup/suppl/doi:10.1073/pnas.1311120110/-/DCSupplemental.

effects of test compounds, the niche of the target cell type—CMs in this case—must be recapitulated in an in vitro model. To engineer this niche, however, key design criteria must be established.

Engineered myocardial tissue models have been used to both elucidate fundamental features of myocardial biology and develop organotypic in vitro model systems for screening. Our previous engineered heart tissue design, which used centimeter-scale collagen scaffolds, had an isotropic matrix architecture (that induced limited CM alignment) and heterogeneity in spatial cell distribution within the volume of the matrix (10). Eschenhagen and coworkers have advanced the field by developing aligned tissue models suitable for some multiwell-plate analytics and that are capable of measuring forces of contraction (22). Together, these and other systems (23, 24) have already proven their utility as models for cell transplantation (25) and drug candidate evaluation (12, 26, 27). We have recently used microfabrication to miniaturize such aligned tissue models into microscale tissues (11). Despite these significant advances, we still do not have established criteria for the design and formulation of 3D microtissues, particularly with respect to input-cell composition, ECM–cell interactions during remodeling mediated by biomechanical forces, accessibility to rapid nondestructive measurements, tissue geometry and cell alignment properties, and, importantly, reproducible electrophysiological properties.

We describe an integrated computational and experimental strategy for the rational design of cardiac microtissues from cardiac differentiated hPSC derivatives. Our so-called cardiac microwire (CMW) system formulated NKX2-5+ cardiomyocytes and CD90+ nonmyocytes with electromechanical stimulation to generate microtissues that reproducibly mimic morphologic and functional properties of adult tissue. CMWs maintained densely aligned architectures and exhibited cell composition-specific remodeling, functional responsiveness to chemicals, and condition-specific gene expression patterns. In proof-of-principle studies, we demonstrated the utility of the platform in modeling tachycardia induced by arrhythmogenic cardiomyopathy, an aspect of cardiac electrophysiology not previously described using a cardiac microtissue model. The design criteria identified herein should accelerate the development of predictive in vitro assays of human heart tissue function.

Results

Finite-Element Modeling Predicts Stress-Mediated Assembly and Alignment of Cardiac Microtissues. Studies have repeatedly shown the impact of a 3D ECM microenvironment on the gene expression and functionality of contained cells, independent of cues from soluble factors. We reasoned that to engineer a more accurate heart cell niche, we would need to transition from 2D substrates to a 3D cell-encapsulating ECM geometry. To achieve this, we exploited the ability of single cells to remodel through their adhesion and contraction of the ECM. We engineered a versatile microfabricated platform and seeding protocol to increase the throughput of our studies (*SI Appendix*, Fig. S1). Although we were successful in generating cardiac microtissues, the geometries and seeding compositions were determined without precise design criteria and, as a result, the formed microtissues were variable and lacked robustness (*SI Appendix*, Fig. S2). Dissociated heart cells encapsulated in a gel will go through several phases: recovery of actin filaments and extension of filopodia, accumulation and assembly of cell-adhesion molecules that help with remodeling, increased expression of gap-junctional and contractile proteins, and finally excitation–contraction coupling, which permits the cardiac tissue to propagate action potentials and contract in unison (28). We hypothesized that by simulating the early remodeling process of gel compaction due to cell-traction forces, we would gain insight into rational design criteria for generating cardiac microtissues.

To provide insight into the stress-mediated formation and contractility of sarcomere filaments in cardiac microtissues, we developed finite-element (FE) models of microtissue and substrate geometries in our platform using a constitutive framework that accounts for the dynamic reorganization and contractility of the cytoskeleton (29). This framework has previously been implemented for the modeling of stress fiber contractility in a range of cell phenotypes (30–33) and for simulation of the response of cells to applied shear (34) and compression (35, 36) loading. Here it is adapted for the simulation of sarcomeric filaments in cardiomyocytes on the basis that both stress fibers and sarcomeric filaments are composed of and operate via actin–myosin interactions. Details of the constitutive model are provided in *SI Appendix*. Briefly, stabilized sarcomeres are predicted when the tension that is actively generated by sarcomeres is structurally supported in the microtissue. A reduction in tension in a given orientation results in a dissociation of actin–myosin contractile filaments in that direction, as illustrated in Fig. 1. As a first step, we explored in silico strategies to spatially predict stress distributions and sarcomere formation within complementary 3D tissue geometries, elucidating the relationship between the local microtissue stress state and sarcomere formation. Two microtissue geometries (Fig. 1) were simulated using our FE-based microtissue contractility model (29): (*i*) a square-shaped microtissue geometry designed to promote the generation of predominantly biaxial intratissue tension forces (BITFs), and (*ii*) a wire-shaped microtissue geometry designed to promote the generation of predominantly uniaxial intratissue tension forces (UNITFs).

Computational results are presented in terms of a nondimensional effective uniaxial stress invariant ($\hat{S}$) and in terms of the level of aligned sarcomere formation (Π) (see *SI Appendix* for model output details). The predicted distribution and alignment of both quantities throughout the BITF and UNITF microtissues are shown in Fig. 2. Peripheral regions of the BITF microtissue experience a uniaxial stress state parallel to the

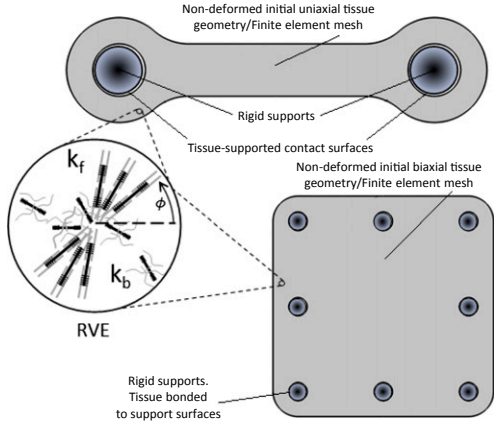

Fig. 1. Overview of experimental and computational strategies for investigating the evolution and contractility of sarcomeric filaments in cardiac microtissues. Two microtissue geometries were simulated using a finite element-based computational model: The first modeled biaxial intratissue tension forces, and the other modeled uniaxial intratissue tension forces, which we termed cardiac microwire. Simulations allowed sarcomeric α-actinin formation in all directions in the finite-element mesh. A cartoon of a representative volume element (RVE) within the finite-element mesh is provided for illustration. The nondimensional sarcomere activation level, $\eta(\phi)$, is computed in all directions (ϕ). A first-order kinetic equation governs the evolution of sarcomeric filaments, whereby filament formation is driven by a signal that decays exponentially with time. The dimensionless constants k_f and k_b govern the rates of formation and dissociation, respectively, of the sarcomere filaments. For additional simulation details, please see *SI Appendix*.

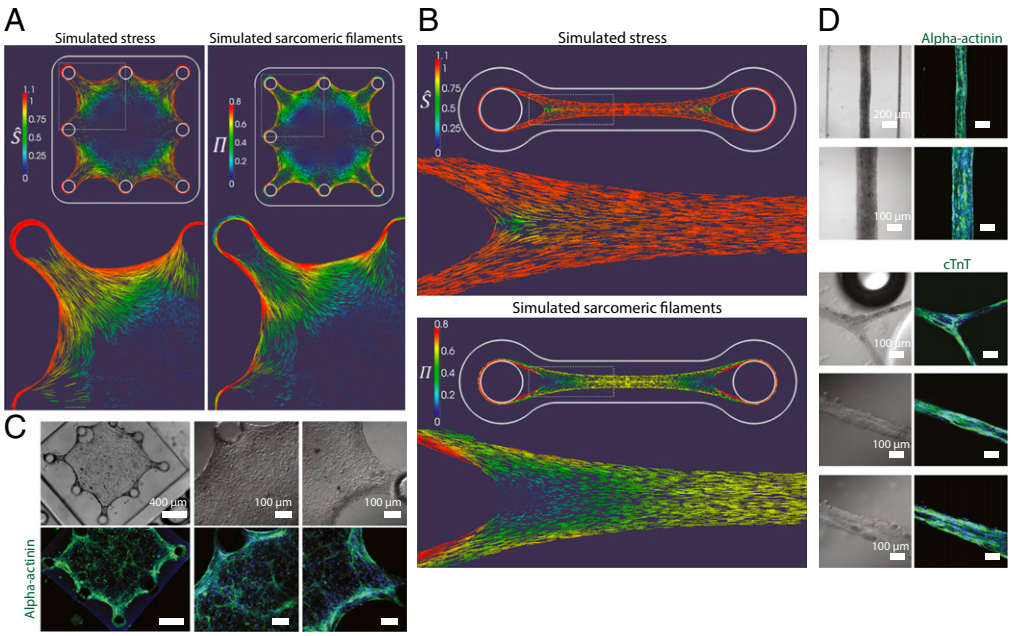

Fig. 2. Self-assembling microtissues composed of heart cells in the ECM induce stress-mediated alignment and patterned expression of sarcomeric filaments. (*A*) Simulation predicts stress (represented by nondimensional effective stress; $\hat{S}$) and sarcomeric expression (represented by Π) in BITF microtissue geometry colocalizing in border regions. (*B*) The simulation predicts stress and sarcomeric α-actinin expression in CMW geometry along the longitudinal axis. (*C*) Immunostaining for sarcomeric α-actinin (green) confirms expression in border regions of BITF microtissue. (*D*) Immunostaining for sarcomeric α-actinin (green; *Upper*) and cardiac troponin T (green; *Lower*) in CMWs confirms sarcomere protein expression in all regions along the longitudinal axis. DAPI-stained nuclei are shown in blue.

microtissue boundaries (Fig. 2*A*, *Left*). In contrast, a biaxial stress state is predicted in the center of the BITF microtissues. As shown in Fig. 2*B*, the distribution and alignment of sarcomeres (Π) corresponds closely to that of $\hat{S}$. In the UNITF microtissue, a highly uniaxial stress state is generated throughout the longitudinal length, producing a uniform regime of uniaxial intratissue tension (Fig. 2*B*, *Upper*). A corresponding uniform distribution of highly aligned sarcomeres is also predicted in this region (Fig. 2*B*, *Lower*). In summary, aligned sarcomere formation is predicted in regions where the local stress state is uniaxial in nature (as $\hat{S} \to 1$). In contrast, sarcomere structures are not computed in regions of the microtissue where the local stress state is biaxial in nature (as $\hat{S} \to 0$). The computed evolution of the stress and sarcomere distributions throughout the microtissue geometries is presented in *SI Appendix*, Figs. S3–S7.

To empirically validate these predictions, we generated substrates as before, but now using the geometries specified in the computational models (*SI Appendix*, Fig. S8 *A* and *B*). We designed disk inserts containing the recessed arrayed poly (dimethylsiloxane) microwells and affixed them inside the bottom wells of a universal 24-well tissue-culture plate (*SI Appendix*, Fig. S8 *C* and *D*). We termed the UNITF microtissue the cardiac microwire. Rat neonatal heart cells were next used to test the system. We observed cells begin to extend filopodia and remodel the surrounding collagen matrix, and within 3 d the microtissues had formed and hit a plateau in morphology. Along with time in culture, we observed that higher concentrations of collagen prolonged the time and extent of microtissue remodeling, as did lowering the input-cell density. As predicted by our model, overall sarcomere expression in the BITF microtissue was observed to be spatially heterogeneous as revealed by immunostaining for cardiac sarcomeric proteins (Fig. 2*C*) in comparison with CMW (Fig. 2*D*). Also predicted by the model, regions exhibiting highly aligned sarcomeres correlated with areas of high stress. Morphologies of CMs in the BITF and CMW microtissues mirrored that of CMs on unaligned and aligned collagen substrates (*SI Appendix*, Fig. S9). In areas where our model predicted alignment due to high uniaxial stress, we observed elongated and oriented cell alignment parallel to modeled localized stress (Fig. 3 *C* and *D*). To test whether the induced alignment in the microtissues was similarly due to topographical cues (via the remodeled and aligned collagen fibrils), we probed the CMW after 3 d of remodeling using the LC-PolScope [Cambridge Research and Instrumentation (CRi)] quantitative birefringence imaging system. The color of the pixel in PolScope micrographs determines the orientation angle of the fibrillar collagen. We confirmed that the fibrillar collagen within the CMW was indeed remodeled and aligned in parallel to the longitudinal axis of the CMW (Fig. 2 *D* and *E*).

These results show that cardiac microtissues under uniaxial tension forces give rise to highly aligned tissues expressing spatially homogeneous contractile proteins that may better mimic cardiac muscle fibers in vitro. However, we were unable to explain the varying degrees of tissue organization (due to remodeling) observed with different input-cardiac cell numbers. To formally investigate this variability of assembly and phenotype in our tissues, we hypothesized that controlling cell composition may mitigate this effect.

Input-Population Composition Impacts Tissue Morphogenesis and Cardiac Gene Expression. To test the hypothesis that cell composition would affect tissue physiology, and to extend our analysis to the formulation of more translationally relevant human cardiac microtissues, we sorted hPSC-derived heart cells to generate tissues with specific input populations consisting of NKX2-5+ cardiomyocytes and CD90+ nonmyocytes (putatively fibroblasts; FBs). We applied our cardiac differentiation protocol to an NKX2-5-GFP reporter human embryonic stem cell (hESC) line that contained the EGFP cDNA inserted into the NKX2-5-GFP locus of HES3 hESC (1, 9). On day 20, we dissociated the hESC–CM aggregates and sorted for both of these populations to high purity (Fig. 4*A*). We generated CMWs of specific CM-to-FB

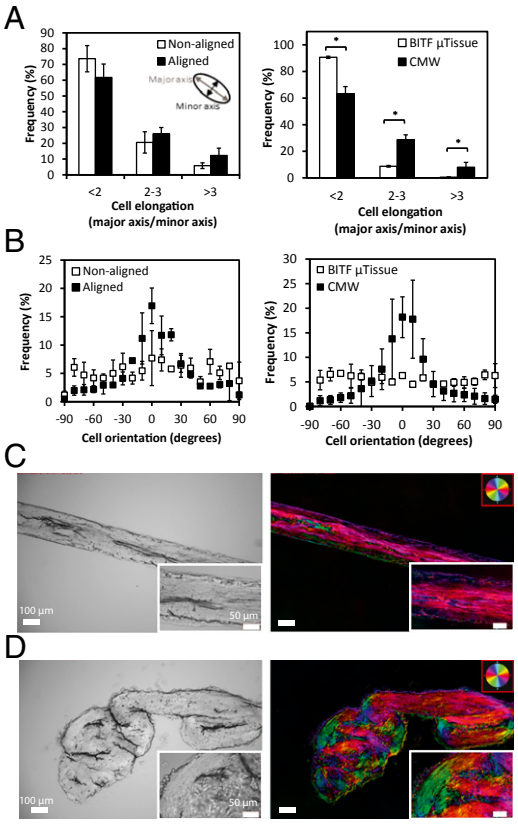

Fig. 3. Aligned tissue architecture can be induced by controlling ECM topography and intratissue mechanical stress. (*A*) Cell elongation of heart cells on pseudo-3D–aligned and unaligned collagen substrates (*Left*) and cell elongation of heart cells in CMWs (*Right*). Measurement of cell elongation is the ratio of the major axis to the minor axis of a cell. (*B*) Cell orientation of heart cells on pseudo-3D–aligned and unaligned collagen substrates (*Left*) and cell orientation of heart cells in CMWs (*Right*). Measurement of cell orientation on pseudo-3D substrates is relative to the direction of alignment of patterned collagen. Measurement of cell orientation in CMWs is relative to the direction of the longitudinal axis. (*C* and *D*) Fibrillar collagen content of CMWs measured with the quantitative birefringence imaging system. Pixel color corresponds to the angle of birefringent fibrillar collagen in CMWs. (*Insets*) Higher-magnification images. (*C*) CMW held taut shows unidirectionally aligned collagen. (*D*) Compacted CMW maintains fibrillar collagen alignment in the direction of the curl. Data are reported as the mean ± SEM. $*P < 0.05$ (Mann–Whitney *U* test).

ratios and controlled spherical reaggregates of the same ratios to exclude effects due to dissociation, flow sorting, and reaggregation. Conditions of the ratios 100:0, 75:25, 50:50, and 25:75 correspond, respectively, to 100%, 75%, 50%, and 25% of NKX2-5-GFP+ cells, with the remainder consisting of CD90+ cells (Fig. 4*B*). Both the CMW and reaggregate microtissues were cultured for 7 d. We observed familiar remodeling kinetics compared with our previous experiments; however, there were clear differences in tissue morphology and physiology between the tissue composition conditions (*SI Appendix*, Table S1). ECM remodeling was observed in all conditions; however, limited gel compaction was observed in 100:0 CMWs, likely due to the lack of FB-associated tissue remodeling (37). As the ratio of CD90+ cells increased, we observed tighter, and more integrated, tissue morphologies under higher apparent tension. CMWs formulated with ratios of 50:50 and 25:75 did not maintain tissue integrity to day 7 and failed due to tension induced by fibrosis. Spontaneous contractions were documented on day 7 for 100:0 and 75:25 CMWs, with limited contractions observed in 50:50 CMWs. Synchronous contractions were only observed in 75:25 and 50:50 CMWs; 100:0 CMWs formed unstable tissue (in both the distal and medial locations) with minimal cell–cell and cell–ECM integration and were undergoing asynchronous contractions (Fig. 4*C*, *Upper Left*). These CMWs contained nonintegrating globular aggregates of cells separated by patches of collagen (*SI Appendix*, Movies S1 and S2). Live-cell imaging of NKX2-5-GFP+ cells in the tissues confirmed that the globular areas were 3D clusters of CMs that had either proliferated into colonies or had conglomerated into clusters over time (Fig. 4*C*, *Lower Left*). As the percentage of CD90+ cells reached 25%, however, the CMWs took on a more robust architecture, with synchronous contractions resembling in vivo-like tissue morphology (Fig. 4*C*, *Right* and *SI Appendix*, Movies S3 and S4). As a result, further electrophysiological measurements on day 7, including conduction velocity, were amenable only in the 75:25 condition.

To determine the spatial localization of the FB population within the tissues before and after tissue formation, we stained and imaged for vimentin (intermediate filaments), a common FB marker. FBs in nondissociated hESC–CM aggregates (Fig. 4*D*, *Insets* and *SI Appendix*, Fig. S10*A*) displayed spatial heterogeneity and fibrotic-like areas within the tissue. In 75:25 CMWs, however, FBs and CMs displayed spatial homogeneity, with evenly dispersed marker expression (Fig. 4*D* and *SI Appendix*, Fig. S10).

Aligned tissue and ultrastructure in the 75:25 CMWs, in comparison with aggregates of the same formulation (*SI Appendix*, Fig. S11), demonstrate the benefits of uniaxial stress with respect to cell spatial organization, apparent cell density, and cell alignment. It is noteworthy that tissue density is higher in CMWs compared with aggregates. Additionally, despite seeding in collagen, there is very little collagen present after the remodeling phase in our CMWs, as evident by lack of collagen (blue) present in our trichrome staining (*SI Appendix*, Fig. S11*B*). Ultrastructure analysis using Transmission Electron Microscopy (TEM) demonstrated increased length and alignment of the myofibrils and sarcomeres, as well as the presence of Z disks and H zones in the CMWs, relative to aggregate controls (*SI Appendix*, Fig. S12).

To study further effects of tissue formulation on tissue development, we examined gene expression of key cardiac maturation markers in our CMWs with respect to aggregates of identical formulation after 7 d in culture. We first looked at control cardiomyocyte markers for determining dilution consistency of input-cell composition. The NKX2-5 gene was the basis of initial CM sorting, and so we used it as both a control and a normalizing factor for measured cardiac-specific genes. As expected, NKX2-5 expression showed a decreasing trend with increasing dilution of CMs in the engineered tissue (Fig. 4*E*), save for the 75:25 aggregate condition. This may perhaps be due to an optimal balance of CM-supportive factors or cell–cell contact (via CD90+ cells) in the matrix-free aggregates compared with the encapsulated CMWs. DDR2, a marker for FBs, showed a significantly increasing trend with decreasing dilution of CD90+ cells. Cx43, expressed in both CMs and FBs, showed consistently level trends. CM marker expression [Signal-regulatory protein α (SIRPA) and cTnT] in both aggregates and CMWs also remained consistently level after being normalized to NKX2-5 (Fig. 4*F*). By effectively controlling for CM number by normalizing all CM-specific genes to NKX2-5, we diminished the differences in CM control marker expression within the four conditions. These results indicate that CMWs maintain their initial dilution consistency, and that there are no significant variations of control CM genes among conditions once tissue-fraction CM number is controlled for.

We next examined the impact of tissue formulation and composition on a panel of CM-specific genes indicative of CM maturation. Markers of CM maturation (ANF, BNP, MYL2, MYL7, MYH6, and MYH7) were also normalized to NKX2-5 expression levels to account for varying CM numbers in the

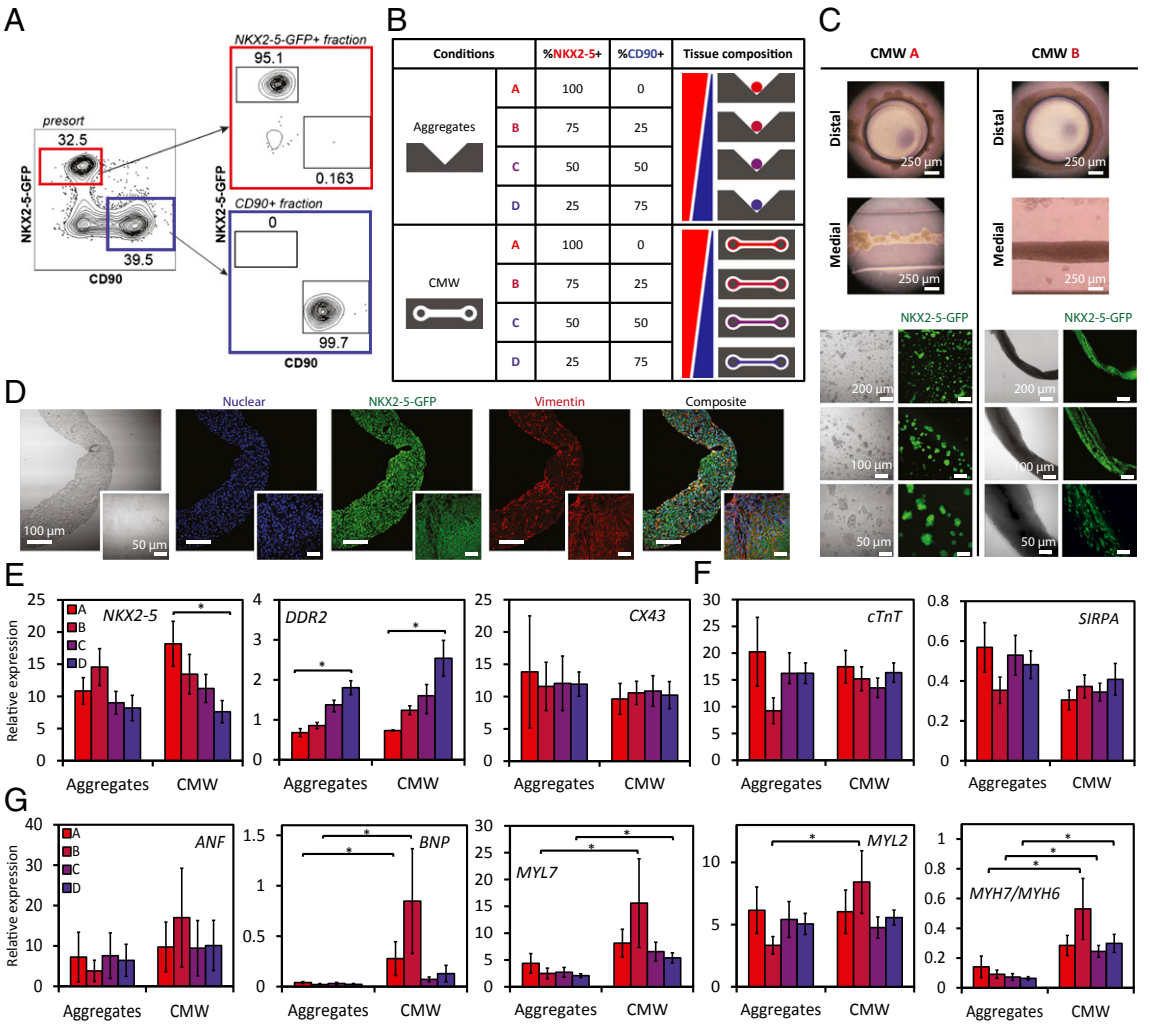

Fig. 4. Controlling input-population compositions of hPSC-derived heart cells guides tissue morphogenesis and levels of maturation in CMWs. (*A*) Flow cytometric cell-sorting plots of NKX2-5-GFP+ (cardiomyocytes) and CD90+ (fibroblasts) mixing experiments. Fluorescence-activated cell sorting of day 20 embryonic stem cell-derived embryoid bodies. EBs were dissociated and sorted for NKX2-5-GFP+ (red gate) and CD90+ (blue gate) fractions (*Left*). Purity control of NKX2-5-GFP+– and CD90+-sorted fractions (*Right*). (*B*) NKX2-5-GFP+ cells and CD90+ cells were sorted from hPSC–CMs and mixed at specific ratios in CMWs and aggregates. (*C*) CMWs composed of pure NKX2-5-GFP+ cells (CMW A) formed tissues consisting of nonintegrating globular colonies of cells (*Left*). Live-cell imaging of the tissues indicated that the globular areas were 3D colonies of CMs. CMWs composed of 75% NKX2-5-GFP+ cells and 25% CD90+ cells (CMW B) produced well-integrated tissue with robust architecture (*Right*). Bright-field live (*Upper*) and fluorescence images are shown (*Lower*). NKX2-5-GFP+ cells are shown in green. (*D*) Immunofluorescence micrographs of CMWs of condition CMW B are shown. (*Insets*) Immunofluorescence micrographs of nondissociated hESC–CM aggregates. DAPI-stained nuclei are shown in blue, NKX2-5-GFP+ cells are shown in green, and vimentin expression is shown in red. (*E*) Gene expression of cardiomyocyte and nonmyocyte control markers shows input-cell composition of CMWs relative to aggregates. (*F*) Gene expression of cardiomyocyte control markers, normalized to NKX2-5 expression, in CMWs relative to aggregates. (*G*) Gene expression of cardiomyocyte maturation markers, normalized to NKX2-5 expression. Conditions A, B, C, and D correspond, respectively, to 100%, 75%, 50%, and 25% NKX2-5-GFP+ cells, with the remainder consisting of CD90+ cells. Data are reported as the mean ± SEM. $*P < 0.05$ (Mann–Whitney *U* test).

mixed population of tissue. Atrial natriuretic factor (ANF), secreted by the atria, and brain natriuretic peptide (BNP), secreted by the ventricle, are cardiac hormones that are involved in normal and diseased heart physiology. Although we did not see an increase of ANF expression in CMWs relative to the control aggregates, significantly increased BNP expression was observed in CMWs in both the 100:0 and 75:25 conditions relative to aggregates. Expression levels of MYL2 (MLC2v) and MYL7 (MLC2a), genes specific to sarcomere structure, were both also observed to be higher in the 75:25 CMWs. Although there were no significant differences in MYH6 (α-MHC) expression between conditions, MYH7 (β-MHC) expression was significantly higher for both the 75:25 and 50:50 conditions. The ratio of MYH7:MYH6, an indicative ratio of maturation, was found to be increased in CMWs for all conditions except the 100:0 condition (Fig. 4*G*). The up-regulation of these genes correlates with the conduction velocity of cardiac muscle, and may be due to the well-integrated and synchronously contracting tissues in the mixed-FB conditions.

It is evident from these gene expression data that there is an interactive effect between the biophysical microenvironment (aggregate versus CMW) and cell composition of tissue (ratio of CM to putative FB). The 75:25 CMW condition was optimal in terms of tissue morphology, and the CMW tissues (relative to the control aggregates) promoted more mature cardiac-specific gene expression. These findings suggest that the combination of a 3D matrix-based microenvironment under uniaxial mechanical stresses with a supporting cell-type fraction (25% CD90+ cells in this case) is a strategic focus in the design criteria of in vitro engineered tissues.

Electrophysiological Assessment of CMWs Indicates Functional Maturation and Disposition to Modulation Using Electrical Stimulation. Our results thus far indicate that tissue phenotype is shaped in part by mechanical forces, input-cell composition, and the composition of the extracellular matrix microenvironment. More specifically, we determined that 75:25 microtissues gave rise to more architecturally robust phenotypes compared with other cell compositions, and our CMWs provided a microenvironment that promoted the increased expression of CM-specific maturation genes. We next wanted to determine whether our 75:25 ratio could be used to study other cardiac tissue properties. Differentiated input populations of CMWs were selected to fall within an acceptable range of 75:25 CMWs (75 ± 10% cTnT+) and were cultured for at least 7 d before being functionally assayed. We focused on studying the excitability, resiliency to high-frequency pacing, and conductivity of our 75:25 CMWs because these have been previously shown to be indicative of electrophysiological improvement in CMs. Excitation threshold and maximum capture rate of CMWs improved significantly compared with hESC–CM aggregates (Fig. 5 *A* and *B*). Maximum capture rate improved even further when CMWs were electrically point-stimulated with a biphasic square wave pulse for 3 d. This was achieved by integrating the two flanking posts within the CMW microwell with platinum wire electrodes to provide electrical point-stimulation capability (*SI Appendix*, Fig. S8*C*). Point stimulation allows for sequential activation of cells and promotes alignment of gap junctions (which also occurs in normal heart maturation) as opposed to field stimulation, which simultaneously stimulates all cells in a tissue. We perturbed CMWs using drugs of known effects and optically mapped their response [transmembrane action potential (AP) and intracellular calcium transient] using voltage- and calcium-sensitive dyes, respectively. Addition of epinephrine (0.1 μg/mL), an adrenergic neurotransmitter, to CMWs increased the activation rate relative to the baseline, whereas adding increasing concentrations of lidocaine (2 μg/mL), an antiarrhythmic drug, reduced and nearly abolished activation (Fig. 5*C*). Adding verapamil (0.25 μg/mL), an L-type Ca^{2+}-channel blocker, reduced the amplitude of calcium waves in CMWs relative to the baseline, and supplementing with epinephrine increased the rate of calcium transients (Fig. 5*D*). We also recorded conduction velocities of CMWs and compared them with healthy (38) and diseased (39) conduction velocities of the human heart (Table 1). Remarkably, CMW conduction velocity (47.4 ± 12.4 cm/s) was found to be comparable to that of a healthy human heart (46.4 ± 2.7 cm/s).

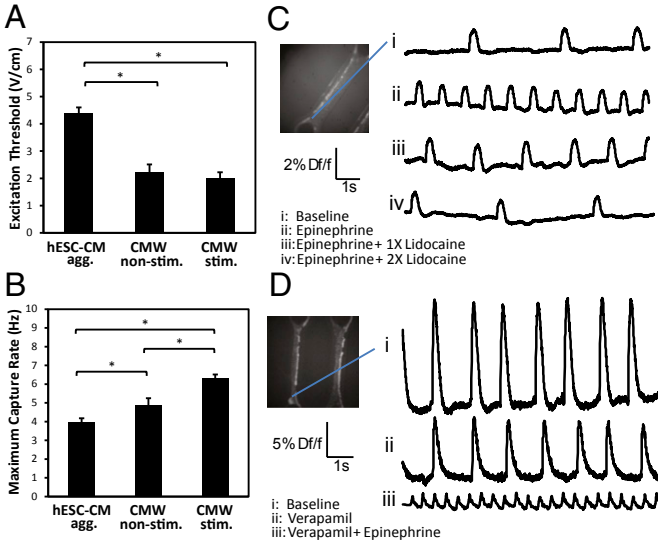

Fig. 5. Functional assessment of CMWs indicates that electrical stimulation improves electrophysiological properties. (*A*) Excitation threshold and (*B*) maximum capture rate of nondissociated hESC–CM aggregates, non-stimulated CMWs, and stimulated CMWs. (*C* and *D*) Optical mapping was used to record transmembrane action potentials and intracellular calcium transients in CMWs. (*C*) Mapping of transmembrane action potentials revealed that epinephrine (0.1 μg/mL), an adrenergic neurotransmitter, increased the activation rate (ii), and lidocaine (2.0 μg/mL), an antiarrhythmic drug, decreased the activation rate (iii and iv) relative to the baseline control (i). (*D*) Mapping of intracellular calcium transients revealed verapamil (0.25 μg/mL), an L-type Ca^{2+}-channel blocker, reduced the amplitude of calcium waves in CMWs (ii) relative to the baseline control (i). Further supplementing with epinephrine increased the rate of calcium transients (iii). Df/f, change in fluorescence intensity relative to fluorescence intensity at baseline. Data are reported as the mean ± SEM. *$P < 0.05$ (Mann–Whitney *U* test).

As an extension, we studied and manipulated the dynamics of activation propagation in CMWs. Typically, in the linear CMW geometry, we observe a normal activation propagation initiate in one of the distal ends, converge, traverse down the longitudinal axis, diverge at the fork at the neck, and terminate at the distal end of the opposite tissue loop (Fig. 6*A* and *SI Appendix*, Movie S5). We next showed the ability to manipulate activation propagation directionality in CMWs using electrical point stimulation. Starting with CMWs with spontaneous activation propagation traversing from left to right (or right to left) (Fig. 6*B*, *Upper* and *SI Appendix*, Movie S6), we reversed the activation propagation direction by electrically pacing from the opposite end (Fig. 6*B*, *Lower* and *SI Appendix*, Movie S7) in all test cases. When the point stimulus was removed, however, the propagation direction reverted to the original direction of spontaneous propagation (*SI Appendix*, Table S2). In some cases of CMWs presenting spontaneous electrical activity, however, we noticed a perturbation that led to unidirectional conduction block at the junction of the medial and distal site (Fig. 6*C* and *SI Appendix*, Movie S8). These unidirectional conduction blocks gave rise to incomplete looped activation propagation trajectories similar to reentrant waves in arrhythmias caused by scar formation; however, they did not reenter the circuit and did not lead to arrhythmia. We then extended our design to better model a reentrant wave in a tachycardic heart by manipulating the geometry of our linear CMWs. CMWs were generated using a circular template substrate to create a ring of tissue mimicking a reentrant wave during tachycardia around functionally unexcitable scar tissue. Circular CMWs (CMW_{circ}) were seeded as previously described and cultured for 14 d before assaying (*SI Appendix*, Movie S9). Reproducibility of CMW_{circ} remodeling was high both within replicates (*SI Appendix*, Movie S10) and between separate experiments. Interestingly, the majority of CMW_{circ} were observed to be in a reentrant state of arrhythmia after 14 d of culture (82% ± 8%) (*SI Appendix*, Table S3 and Movie S11) and the rest were in normal rhythms (*SI Appendix*, Movie S12). Electrophysiological assessment revealed spontaneous infinite loop-like cycles of activation propagation traversing the ring as expected (Fig. 6*D*). Trace recordings indicate a high-frequency activation rate with no rest period. Please see *SI Appendix*, Movie S13 for a video of multiple cycles of activation propagation. We next aimed to "defibrillate" the CMW_{circ} from a reentrant state of arrhythmia to a normal rhythm state. Using carbon electrodes spaced 1 cm apart, CMW_{circ} were field-stimulated at 10 V for 3 s. After a 2- to 3-s period of inactivity, the CMW_{circ} recovered to a normal rhythm (~1 Hz) in all test cases (Fig. 6*E* and *SI Appendix*, Movie S14). Following culture of an additional 7 d, the majority of CMW_{circ} remained in normal rhythm (95% ± 4%), while a small percentage degenerated back to an arrhythmic state (5% ± 4%). We have shown here that by simply modulating the geometry of our tissue, we can recapitulate basic elements of a disease model—in this case, tachycardia in a model of arrhythmogenic cardiomyopathy.

Table 1. Comparison of conduction velocities of native human heart tissue and the CMW system

Subject	Conduction velocity, cm/s	Ref.
Human CMWs	47.4 ± 12.4	—
Healthy human heart	46.4 ± 2.7	(38)
Healthy human heart, Purkinje fibers	~2,000	(38)
Cardiomyopathic human heart during pacing	41 (min)–87 (max)	(39)
Cardiomyopathic human heart during ventricular fibrillation	25 ± 4.0	(39)

Values of normal and pathophysiological conduction velocities of the human heart obtained from the literature are shown. Values for CMWs were measured from three separate experiments via optical-mapping techniques. Microengineered CMWs were found to exhibit conduction velocities on par with the epicardium of a healthy human heart. Data are reported as the mean ± SEM.

Discussion

Cardiac tissue engineering, whether for transplantation or in vitro modeling, requires key design criteria and processes for robust and reproducible results. The design methods and results presented here are, to our knowledge, a unique method of combining computational approaches with tissue design and "bottom-up" construction of hPSC-derived heart tissue using transcription- and surface marker-delineated heart cell populations. We demonstrate the importance of understanding and modulating (*i*) the biomechanical microenvironment and associated effects on spatial organization of structural and functional proteins during tissue growth in three dimensions, (*ii*) the cell composition of tissue and subsequent cell–cell and cell–ECM interactions, and, finally, (*iii*) the effect of geometry on tissue physiology. Previous studies proposing hPSC–CM–based in vitro models have not accounted for effects of intratissue stresses in the design phase with the aid of computational models simulating actin polymerization and myosin phosphorylation. Additionally, in previous studies, cell composition is usually not precisely engineered and, in the cases where input population was determined, none have studied the effects of ratio-based formulations of cocultured functional and stromal cell types.

In this study, we have adapted an FE model of tissue contractility via the active remodeling of stress fibers to describe the evolution and contractility of sarcomeric filaments in in vitro cardiac microtissues. With this unique approach in determining design criteria for engineered tissue, we have demonstrated the importance of uniaxial stress-mediated sarcomere filament formation for building tissue expressing spatially homogeneous sarcomeric protein. Certainly insight from such in silico models, with the capability to recapitulate the organization and remodeling of the cytoskeleton, can have significant impact in the understanding and modulation of tissue morphogenesis in tissue-engineering applications.

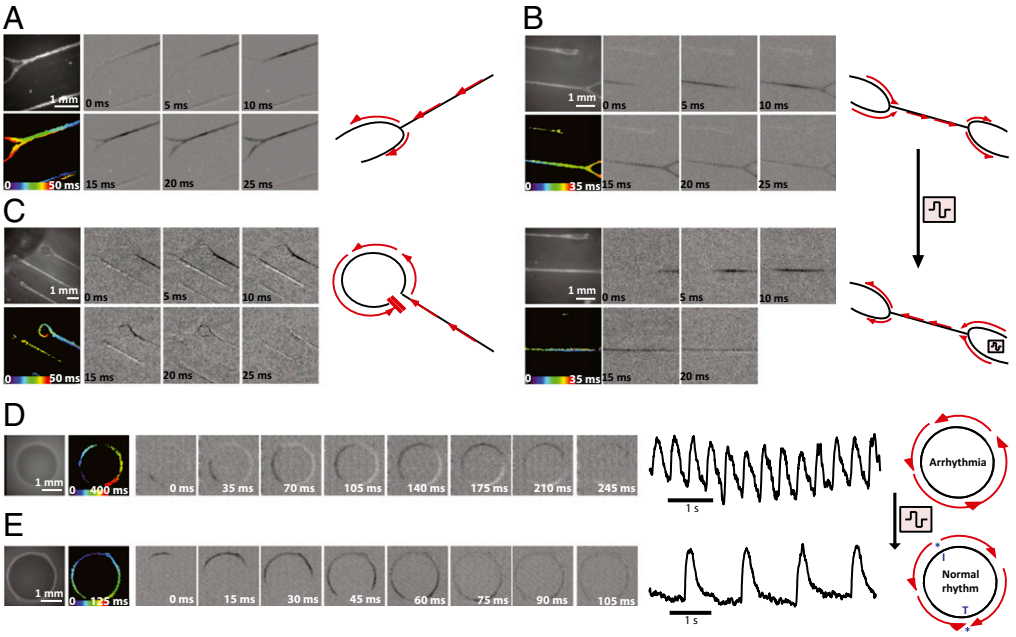

Fig. 6. CMW activation propagation is disposed to directional modulation using electrical stimulation. (*A*) Activation propagation of normal CMWs. Each panel depicts a time lapse of the activation propagation along the longitudinal axis of the CMW. Phase-contrast image of CMWs, isochronal map, and timescale are indicated. (*B*) Direction of spontaneous activation propagation of normal CMWs (*Upper*) can be reversed using electrical point stimulation (*Lower*). (*C*) Activation propagation of CMWs observed to be obstructed by a conduction block, resulting in an incomplete reentrant wave-like system. (*D*) CMWs generated using a circular substrate (CMW_{circ}) designed to create a ring of tissue mimicking a reentrant wave during arrhythmia. Assessment revealed spontaneous infinite loop-like cycles of activation propagation traversing the ring; one cycle is shown. Signal tracings show multiple cycles. (*E*) Normal rhythm was observed in CMW_{circ} after defibrillation. An electrical field stimulation of 10 V was used to defibrillate arrhythmias in CMW_{circ} geometries to a normal rhythm. Signal tracings show multiple cycles. The initiation site in blue (I*) indicates the starting location of impulse propagation, and the termination site in blue (T*) indicates the final location of impulse propagation.

Importantly, results from our sorting studies highlight the importance of tissue composition due to improved functional assembly in CMWs composed of 75% NKX2-5+ and 25% CD90+ cells and improved mature cardiac gene expression in CMWs (relative to aggregates in select compositions). We report increased gene expression levels in CMWs of key cardiac maturation markers, including genes implicated in sarcomere structure, as well BNP, which increases during the fetal heart gene program when organogenesis commences (40). We speculate that there may be high expression of integrins and adhesion proteins in the CD90+ cells that promotes ECM remodeling and, as a direct result, bring cells together during tissue contraction to promote cell–cell contact, which has been shown to facilitate maturation signaling (41–43). Putatively fibroblasts, these CD90+ cells may also secrete growth factors such as bFGF and VEGF. Additionally, the remodeling may provide mechanotransductive cues such as tension forces, and in turn induce CM elongation and alignment.

In our optimal CMW system, we report conduction velocities on par with that of a healthy adult heart. We also show the capability of modulating activation propagation direction using electrical stimulation. Our ability to generate arrhythmic models, and then to defibrillate the arrhythmia to a normal rhythm, demonstrates the CMW_{circ} system's versatility and potential as a disease model and may serve as a platform to test the impact of antiarrhythmic drugs. Previous in vitro models of arrhythmogenesis do not exhibit the reproducibility and robustness of the CMW_{circ} system, and additionally are not derived from hPSCs constructed in 3D tissue. Conversely, we plan to use the normal rhythm model as a tool to screen for proarrhythmic compounds.

The complete set of microenvironmental parameters of the myocardial niche was not recapitulated in our system, and so may likely explain our shortcoming of reaching some outputs from our CMWs that parallel that of native heart tissue. Indeed, there are other cell types and tissues not accounted for, including endothelial and immune cells in our system, along with their associated paracrine signaling. Nonetheless, our current model contains a basic subset of the elements needed to carry forward a sophisticated high-content screen of small molecules.

The versatility and customizability of the CMW platform allows for a variety of cell types and geometries to be generated en masse. For example, using the CMW_{circ} geometry, noncardiac 3D tissue cocultures can be spatially engineered whereby an initial stromal cell type, endothelial cells for instance, can be seeded and permitted to remodel. Next, a second functional cell can be seeded circumferentially around the endothelium to create concentrically adjacent tissue types. Intertissue interactions between the adjacent tissue types can then be studied in a 3D tissue-like environment.

In conclusion, we demonstrate a bottom-up approach for the engineering of cardiac microtissues with the consideration of key design criteria. The robustness, flexibility, and increased throughput of our CMW platform highlight its potential as a powerful tool as an in vitro model for the screening of small molecules toward heart-regeneration therapies. Next-generation tissue-engineering approaches, to be effective, need to integrate these self-organization–based design criteria to build functional and reproducible tissue.

Materials and Methods

Isolation of Rat Neonatal Cardiomyocytes. Rat neonatal cardiomyocytes were isolated as previously reported (10). Briefly, hearts were isolated from 1- to 2-d-old neonatal Sprague–Dawley rats using protocol approved by the University of Toronto Committee on Animal Care. Rat hearts of one or two litters of ~13 pups per litter were aseptically excised and placed in cold HBSS (Sigma), washed several times with HBSS, and quartered. Quartered hearts were then incubated overnight at 4 °C in a 0.06% (wt/vol) solution of trypsin (Gibco) in HBSS on an orbital shaker at 0.5 × *g* (Labent Orbit LS; Mandel). After 14–16 h, hearts were washed with CM culture medium [high-glucose (4.5 g/L) DMEM with L-glutamine (Gibco) supplemented with 10% (vol/vol) FBS (Gibco), 1% (vol/vol) penicillin/streptomycin (Gibco), and 1% (vol/vol) Hepes (Gibco)] and subjected to a series of five digests (8 min, 37 °C, 1 × *g*) in a 0.1% (wt/vol) solution of collagenase type II (Worthington) in HBSS. The supernatant of each digest was collected, centrifuged (5 min, 150 × *g*), and resuspended in CM medium. Cells were preplated for 60 min on tissue-culture polystyrene T75 flasks (BD Falcon) to enrich for cardiomyocytes (nonadherent cells). The supernatant was collected, and cell number was determined via trypan blue (Gibco) exclusion.

Cardiac Differentiation of Human Embryonic Stem Cells. Cardiac differentiation of human embryonic stem cells was carried out as reported previously (44). In this study, the HES2 (ES Cell International) hESC line was used. The hESCs were maintained and expanded as described previously. Briefly, HES2 cells were passaged (up to five times) on mouse embryonic feeders (MEFs) for 6 d in HES2 maintenance media (80% DMEM/F12, 20% KOSR, 20 ng/mL bFGF, 0.5% P/S, 1% NEAA, 1% BME); media were changed daily. Cells were maintained in normoxia at 37 °C in a 5.0% CO_2 atmosphere. The cells were then trypsinized along with MEFs and plated onto Matrigel (diluted 1:30)-coated plates at a split ratio of 1:3 for MEF depletion. After 2 d of MEF depletion, HES2 cells were again trypsinized and seeded into AggreWells (Stemcell Technologies) manufactured in-house to form human embryoid bodies (hEBs). The hEBs were generated using 400-μm microwell poly (dimethylsiloxane) (PDMS) inserts cast from a silicon master mold. The inserts were cut and glued into 24-well tissue-culture plates and then sterilized using ethanol. The microwells were then coated with 5% pluronic acid for at least an hour and washed with PBS before cell seeding. A single-cell suspension of aggregation media containing base media and T0 (day 0 of differentiation) cytokines supplemented with ROCK inhibitor Y-27632 was then seeded into the wells and allowed to aggregate overnight after centrifuging at 200 × *g*. Cells were maintained in hypoxia at 37 °C in a 5.0% CO_2 and 5.0% O_2 atmosphere. After 24 h, hEBs were formed and aggregation media were exchanged for T1 media. On day 4, hEBs were removed from the AggreWells and placed in low-cluster six-well plates (Nunc). Corresponding media for T4, T8, and T12 were freshly made and exchanged. On T12, cells were returned to normoxia at 37 °C in a 5.0% CO_2 atmosphere. Media were replaced every 8 d onward.

Microfabrication. Masks for master patterning were designed using AutoCAD (Autodesk) and printed at a resolution of 20,000 dots per inch (CAD/Art Services). Microfluidic cell-culture devices were fabricated at the Emerging Communications Technology Institute cleanroom at the University of Toronto. Briefly, piranha-washed 3 × 5-inch clean glass slides (Corning) were given a brief wash in acetone and blow-dried under a clean stream of nitrogen gas. A seed layer of SU-8-5 (MicroChem; 7 μm high) was spin-coated onto the surface to allow for feature-layer bonding. Following a dehydration bake for 20 min on a 100-°C hot plate, the slides were then cooled to 65 °C and removed from the hot plate to return to room temperature. The seed layer was exposed to UV and postbake was intiated as before. The slides with the seed layers had two spin-coated layers of SU-8-50 (MicroChem) applied sequentially (including pre- and postbakes) to reach a feature-layer height of 300 μm. The designed mask was UV-exposed onto the master with a 300-μm–high feature layer. Postbake, sufficient time was allowed for cooling. Immersion in developer (MicroChem) on a sonicator or orbital shaker was done until un–cross-linked SU-8 was washed away thoroughly. Masters were oven-baked for 3 d at 75 °C to allow proper bonding of the feature layer to the glass slide. Masters were silanized in a desiccator overnight. Primary replicates were manufactured by molding PDMS (Dow Corning) on SU-8 masters at 65 °C overnight. Replicates were modified under a stereomicroscope, and a negative master was molded using polyurethane (SmoothCast). Final substrates were then PDMS-molded from these negative masters and outfitted onto a 24-well tissue-culture plate.

Generation, Cultivation, and Imaging of Cardiac Microtissues. Either rat neonatal CMs or hESC-derived CMs were suspended in a collagen master mix and seeded into cardiac microtissue wells at a density of 0.5×10^6 cells per mL. Microwell substrates were prepared by sterilizing with ethanol and washing and coating with 5% (wt/vol) pluronic acid for at least an hour each. During the coating, rat neonatal CMs and/or hESC-derived CMs were prepared. Aggregates from hESC–CM differentiation were put in collagenase type II (1 mg/mL; Sigma) for 1 h with DNase in an incubator. Aggregates were then immersed in 0.25% trypsin for 5–10 min with DNase. Aggregates were then immersed in STOP solution (50% FBS and 50% DMEM/F12) and triturated with a 20-gauge syringe 10 times. Once aggregates were single cells, they were immersed in STAIN solution (10% FBS and 90% DMEM/F12) and counted. The collagen master mix was prepared by combining the following:

10× M199 (Gibco), Glutamax (Gibco), Collagen 1 (3.66 mg/mL) (BD Biosciences), glucose (0.3 g/mL) (Gibco), NaOH (Sigma), $NaHCO_3$ (0.075 g/mL) (Sigma), Hepes (Gibco), GFR Matrigel (BD Biosciences), and ddH_20 at appropriate ratios for the desired collagen concentrations. The collagen master mix was constantly kept on ice under 4 °C to prevent premature cross-linking. Finally, 500 μL of master mix was pipetted into each well (of a 24-well plate) and centrifuged at high speed (300 × *g*) to eliminate bubbles. The centrifuge was maintained at an ice-cold temperature. The cell-laden collagen (an additional 250 μL per well) was prepared and pipetted/mixed into each well to a final cell density of 500,000 cells per well (the final volume in each well was 750 μL). The entire plate was centrifuged (200 × *g*) to force the cells into microwell recessions. Excess cell-laden collagen in each well was carefully and slowly aspirated to leave pockets of cell-laden collagen in each microwell. The entire plate was placed in a normoxic incubator for 15 min. After 15 min, 1 mL of cell-culture media was added slowly so as not to disrupt the polymerized collagen microtissues. Media were exchanged every 4 d. Microtissues remodel between 1 and 3 d depending on input-cell composition. Imaging of microtissues was done in situ. Samples were fixed, permeabilized, and stained inside the microwells and imaged using a fluorescence microscope.

Electrical Stimulation and Functional Analysis. For electrical point stimulation, microwells were embedded with 0.005-inch–diameter platinum wires (99.99% purity; A-M Systems) and hooked up to a commercial stimulator (Grass S88X; Astro-Med). After 72 h of cultivation without electrical stimulation, the microtissues to be stimulated were stimulated with biphasic, square pulses 1 ms in duration, with a threshold amplitude of 6 V (field strength of 6 V/cm) and a frequency of 1 Hz for the remainder of cultivation (4 d). The stimulation voltage was selected to induce synchronous construct contractions. Constructs were held in place within the PDMS substrate.

Tissue function was established by measuring excitation threshold (ET), the minimum voltage required to pace the tissue simultaneously, and maximum capture rate (MCR), the maximum stimulation rate at which the construct can be induced to beat simultaneously, at 7 d after cell seeding. Tissue constructs or CM aggregates were individually placed between a pair of carbon electrodes in stimulation chambers (autoclaved before use). ET (V/cm) was measured by stimulating the tissue with square pulses of 2-ms pulse width at a frequency of 1 or 2 Hz and gradually increasing the output voltage of the stimulator until >80% of the tissue was beating synchronously with the stimulator output. MCR was measured by setting the output voltage at 12 V and increasing frequency until >80% of the tissue was no longer synchronously beating with the driving signal. All measurements were taken using an Olympus 1X2-UCB inverted fluorescence microscope housed in an environmental chamber (Solent Scientific) maintained at a temperature of 37 °C and equipped with a Retiga camera (QImaging).

Flow Cytometry and Cell Sorting. For flow cytometric analysis, aggregates were dissociated using collagenase treatment and trypsin and immediately fixed with 4% paraformaldehyde (PFA) overnight at 4 °C. They were then permeabilized at room temperature with 100% methanol for 2 min. Primary antibody was added after a 2% HF wash. It was then incubated at room temperature for 20 min. Next, the sample was washed with HF and the secondary antibody was added for another 20 min at room temperature. Last, the sample was washed again to be ready for flow cytometric analysis. The samples were always kept on ice before measurement by flow cytometer.

For flow cytometric cell sorting, EBs were dissociated as previously described (45). Cells were stained with anti-CD90 allophycocyanin (BD Pharmingen; 1:500). Stainings were carried out in PBS with 10% FCS on ice. The cells were sorted using a FACSAria TMII (BD Biosciences) cell sorter (SickKids-University Health Network Flow Cytometry Facility). Data were analyzed using FlowJo software (Tree Star).

Immunostaining and Image Analysis. Microtissues were washed with PBS and fixed for 24 h with 4% PFA at 4 °C. They were then permeabilized in 0.1% Triton X in blocking solution (normal donkey serum). Primary antibody was then added for 3 d at 4 °C. Last, the microtissues were washed three times and stained with the appropriate secondary antibody (Alexa Fluor series) and with DAPI for nuclear staining overnight at 4 °C. Each incubation step was preferably performed on a rocker table. Before imaging, the sample was washed three times and resuspended in 2% HF. Samples were imaged using confocal microscopy (FV1000 laser scanning confocal microscope; Olympus). All image analysis was done using custom macros built in ImageJ (National Institutes of Health) (cell alignment and elongation analysis, and total cell-marker expression enumeration).

Quantitative Real-Time PCR. Total RNA was prepared with the RNAqueous-Micro Kit (Ambion) and treated with RNase-free DNase (Ambion). RNA (500 ng–1 pg) was reverse-transcribed into cDNA using random hexamers and Oligo(dT)s with SuperScript III Reverse Transcriptase (Invitrogen). Quantitative PCR was performed on a MasterCycler EP RealPlex (Eppendorf) using the QuantiFast SYBR Green PCR Kit (Qiagen). Expression levels were normalized to the housekeeping gene *TATA box binding protein* (*TBP*). The oligonucleotide sequences can be found in *SI Appendix*.

Optical Mapping. For optical measurements, microtissues were stained with 5 mM voltage sensitive dye di-4-ANEPPS (Invitrogen) voltage-sensitive dye for 20 min, followed by three washouts with fresh warm Tyrode's solution (Sigma-Aldrich) adjusted to pH 7.4. The temperature was kept constant at 37 °C using a block incubator. Dye fluorescence was recorded using a microscope mapping system (Ultima; SciMedia). The system included a CMOS camera with a 1-cm sensor (100 × 100 pixels) attached to a custom-built microscope using a Plan Apo objective and condensing lenses (Leica Microsystems), giving a magnification of 1.5×. The spatial resolution was 63 μm per pixel. The fluorescence was excited using a xenon light source (Moritek) and a 530-nm green filter (Semrock), and the emission signal was long pass-filtered using a 610-nm red filter. Tissue constructs were point-stimulated at a 1,000-ms cycle length using a bipolar electrode made with two fine silver wires ((American Wire Gauge 32; A-M Systems Inc.) 32) inserted into a large stainless steel needle mounted on a micromanipulator. Spontaneous tissue beating was also recorded, in addition to responses to frequency sweep from 1 to 5 Hz. Local activation times were measured at the peak of dF/dT (first derivative of fluorescence) for each pixel. Activation maps were constructed for a selected beat. Conduction velocity was calculated at each location using activation times of nine neighboring sites. Conduction velocity values from all sites were used to calculate the average conduction velocity across the construct surface; minimum and maximum values were also noted. Phase-contrast images of microtissue surfaces were taken before optical mapping to correlate tissue architecture geometry with conduction velocity.

Statistical Analysis and Data Representation. Statistical significance was computed using the Mann–Whitney *U* test. All error bars represent the SEM of three or more biological replicates. Asterisks indicate statistical significance between conditions of $P < 0.05$. All data analyses, including graphical representations, were performed using Excel (Microsoft); statistical analysis was performed using custom macros written in R programming language (R Development).

ACKNOWLEDGMENTS. We thank Ting Yin, Patrick Lai, Marjan Kusha, Joshua Lopes, Samuel McEwen, and Christopher Yip for technical assistance, and Geoff Clarke for critical reading of this manuscript. We acknowledge the following funding sources: Ontario Research Fund - Great Lakes 2 Grant (to M.R. and P.W.Z.), Heart & Stroke Foundation of Ontario Grant (to P.W.Z.), and Silver Creek Pharmaceuticals. P.W.Z. is the Canada Research Chair in Stem Cell Bioengineering. M.R. is the Canada Research Chair in Functional Cardiovascular Tissue Engineering. J.P.M. acknowledges support from Science Foundation Ireland and the Science Foundation Ireland/Higher Education Authority Irish Centre for High-End Computing. N.T. receives funding from a Heart and Stroke Foundation of Canada/Canadian Institutes of Health Research Doctoral Research Award and from a Natural Sciences and Engineering Research Council Microfluidic Applications and Training in Cardiovascular Health Scholarship.

1. Elliott DA, et al. (2011) NKX2-5(eGFP/w) hESCs for isolation of human cardiac progenitors and cardiomyocytes. *Nat Methods* 8(12):1037–1040.
2. Burridge PW, Keller G, Gold JD, Wu JC (2012) Production of de novo cardiomyocytes: Human pluripotent stem cell differentiation and direct reprogramming. *Cell Stem Cell* 10(1):16–28.
3. Zhang J, et al. (2012) Extracellular matrix promotes highly efficient cardiac differentiation of human pluripotent stem cells: The matrix sandwich method. *Circ Res* 111(9):1125–1136.
4. Xu C, et al. (2011) Efficient generation and cryopreservation of cardiomyocytes derived from human embryonic stem cells. *Regen Med* 6(1):53–66.
5. Zhu W-Z, Van Biber B, Laflamme MA (2011) Methods for the derivation and use of cardiomyocytes from human pluripotent stem cells. *Methods Mol Biol* 767: 419–431.
6. Lian X, et al. (2012) Robust cardiomyocyte differentiation from human pluripotent stem cells via temporal modulation of canonical Wnt signaling. *Proc Natl Acad Sci USA* 109(27):E1848–E1857.
7. Kattman SJ, et al. (2011) Stage-specific optimization of activin/nodal and BMP signaling promotes cardiac differentiation of mouse and human pluripotent stem cell lines. *Cell Stem Cell* 8(2):228–240.

8. Uosaki H, et al. (2011) Efficient and scalable purification of cardiomyocytes from human embryonic and induced pluripotent stem cells by VCAM1 surface expression. *PLoS One* 6(8):e23657.
9. Dubois NC, et al. (2011) SIRPA is a specific cell-surface marker for isolating cardiomyocytes derived from human pluripotent stem cells. *Nat Biotechnol* 29(11): 1011–1018.
10. Dengler J, et al. (2011) Engineered heart tissue enables study of residual undifferentiated embryonic stem cell activity in a cardiac environment. *Biotechnol Bioeng* 108(3):704–719.
11. Boudou T, et al. (2012) A microfabricated platform to measure and manipulate the mechanics of engineered cardiac microtissues. *Tissue Eng Part A* 18(9-10):910–919.
12. Schaaf S, et al. (2011) Human engineered heart tissue as a versatile tool in basic research and preclinical toxicology. *PLoS One* 6(10):e26397.
13. Kean TJ, et al. (2012) Development of a peptide-targeted, myocardial ischemia-homing, mesenchymal stem cell. *J Drug Target* 20(1):23–32.
14. Iyer RK, Odedra D, Chiu LL, Vunjak-Novakovic G, Radisic M (2012) Vascular endothelial growth factor secretion by nonmyocytes modulates Connexin-43 levels in cardiac organoids. *Tissue Eng Part A* 18(17-18):1771–1783.
15. Panáková D, Werdich AA, Macrae CA (2010) Wnt11 patterns a myocardial electrical gradient through regulation of the L-type Ca(2+) channel. *Nature* 466(7308):874–878.
16. Kurazumi H, et al. (2011) The effects of mechanical stress on the growth, differentiation, and paracrine factor production of cardiac stem cells. *PLoS One* 6(12):e28890.
17. Thavandiran N, Nunes SS, Xiao Y, Radisic M (2013) Topological and electrical control of cardiac differentiation and assembly. *Stem Cell Res Ther* 4(1):14.
18. Kim D-H, et al. (2010) Nanoscale cues regulate the structure and function of macroscopic cardiac tissue constructs. *Proc Natl Acad Sci USA* 107(2):565–570.
19. Feng Y, Yu X-Y, Wang Y (2012) Recent concepts for the roles of progenitor/stem cell niche in heart repair. *Am J Cardiovasc Dis* 2(1):75–83.
20. Gupta MK, et al. (2011) Combinatorial polymer electrospun matrices promote physiologically-relevant cardiomyogenic stem cell differentiation. *PLoS One* 6(12):e28935.
21. Sassoli C, et al. (2011) Mesenchymal stromal cells affect cardiomyocyte growth through juxtacrine Notch-1/Jagged-1 signaling and paracrine mechanisms: Clues for cardiac regeneration. *J Mol Cell Cardiol* 51(3):399–408.
22. Hansen A, et al. (2010) Development of a drug screening platform based on engineered heart tissue. *Circ Res* 107(1):35–44.
23. Vandenburgh H, et al. (2009) Automated drug screening with contractile muscle tissue engineered from dystrophic myoblasts. *FASEB J* 23(10):3325–3334.
24. Grosberg A, Alford PW, McCain ML, Parker KK (2011) Ensembles of engineered cardiac tissues for physiological and pharmacological study: Heart on a chip. *Lab Chip* 11 (24):4165–4173.
25. Song H, et al. (2010) Interrogating functional integration between injected pluripotent stem cell-derived cells and surrogate cardiac tissue. *Proc Natl Acad Sci USA* 107(8): 3329–3334.
26. Kraushaar U, et al. (2012) Cardiac safety pharmacology: From human ether-a-gogo related gene channel block towards induced pluripotent stem cell based disease models. *Expert Opin Drug Saf* 11(2):285–298.
27. Braam SR, et al. (2010) Prediction of drug-induced cardiotoxicity using human embryonic stem cell-derived cardiomyocytes. *Stem Cell Res (Amst)* 4(2):107–116.
28. Radisic M, et al. (2004) Functional assembly of engineered myocardium by electrical stimulation of cardiac myocytes cultured on scaffolds. *Proc Natl Acad Sci USA* 101(52): 18129–18134.
29. Deshpande VS, McMeeking RM, Evans AG (2006) A bio-chemo-mechanical model for cell contractility. *Proc Natl Acad Sci USA* 103(38):14015–14020.
30. Pathak A, Deshpande VS, McMeeking RM, Evans AG (2008) The simulation of stress fibre and focal adhesion development in cells on patterned substrates. *J R Soc Interface* 5(22):507–524.
31. McGarry JP, et al. (2009) Simulation of the contractile response of cells on an array of micro-posts. *Philos Trans A Math Phys Eng Sci* 367(1902):3477–3497.
32. Deshpande VS, McMeeking RM, Evans AG (2007) A model for the contractility of the cytoskeleton including the effects of stress-fibre formation and dissociation. *Proc R Soc A* 463(2079):787–815.
33. Legant WR, et al. (2009) Microfabricated tissue gauges to measure and manipulate forces from 3D microtissues. *Proc Natl Acad Sci USA* 106(25):10097–10102.
34. Dowling EP, et al. (2012) The effect of remodelling and contractility of the actin cytoskeleton on the shear resistance of single cells: A computational and experimental investigation. *J R Soc Interface* 9(77):3469–3479.
35. Dowling EP, Ronan W, McGarry JP (2013) Computational investigation of in situ chondrocyte deformation and actin cytoskeleton remodelling under physiological loading. *Acta Biomater* 9(4):5943–5955.
36. Ronan W, Deshpande VS, McMeeking RM, McGarry JP (2012) Numerical investigation of the active role of the actin cytoskeleton in the compression resistance of cells. *J Mech Behav Biomed Mater* 14:143–157.
37. Porter KE, Turner NA (2009) Cardiac fibroblasts: At the heart of myocardial remodeling. *Pharmacol Ther* 123(2):255–278.
38. Durrer D, et al. (1970) Total excitation of the isolated human heart. *Circulation* 41(6): 899–912.
39. Nanthakumar K, et al. (2007) Optical mapping of Langendorff-perfused human hearts: Establishing a model for the study of ventricular fibrillation in humans. *Am J Physiol Heart Circ Physiol* 293(1):H875–H880.
40. Cameron VA, Ellmers LJ (2003) Minireview: Natriuretic peptides during development of the fetal heart and circulation. *Endocrinology* 144(6):2191–2194.
41. Uosaki H, et al. (2012) Direct contact with endoderm-like cells efficiently induces cardiac progenitors from mouse and human pluripotent stem cells. *PLoS One* 7(10): e46413.
42. Ma Z, et al. (2013) Mesenchymal stem cell-cardiomyocyte interactions under defined contact modes on laser-patterned biochips. *PLoS One* 8(2):e56554.
43. McSpadden LC, Nguyen H, Bursac N (2012) Size and ionic currents of unexcitable cells coupled to cardiomyocytes distinctly modulate cardiac action potential shape and pacemaking activity in micropatterned cell pairs. *Circ Arrhythm Electrophysiol* 5(4): 821–830.
44. Bauwens CL, et al. (2011) Geometric control of cardiomyogenic induction in human pluripotent stem cells. *Tissue Eng Part A* 17(15-16):1901–1909.
45. Sharma P, Shathasivam T, Ignatchenko V, Kislinger T, Gramolini AO (2011) Identification of an FHL1 protein complex containing ACTN1, ACTN4, and PDLIM1 using affinity purifications and MS-based protein-protein interaction analysis. *Mol Biosyst* 7(4):1185–1196.

Supplementary Information Appendix

SUPPLEMENTARY FIGURE LEGENDS

Fig. S1. A PDMS substrate is replicated from a microfabricated master, and then modified with tapered heads. A negative polyurethane-based master is generated and used as the final master. Substrates are then prepared in 24-well plates and sterilized. Cell laden collagen is centrifuged into recessions of microwells and allowed to remodel into densely-packed tissue.

Fig. S2. Microtissue formation in microfabricated platforms. (A) Cells are seeded and centrifuged into recessions and allowed to remodel to form microtissues based on node geometries. (B) Platforms with deflecting posts can be used to measure forces exerted by tissue and to also constrain tissue remodeling at various degrees. (C) Microtissues can be arrayed on a common surface to increase samples per well. (D, E) Microtissues can be fixed, permeablized, stained, and imaged in-situ within the microtissue seeding substrate. Immunofluorescence shows Phalloidin-stained actin filaments (red), Cardiac TroponinT (green) and DAPI-stained nuclei (blue).

Fig. S3. Experimental and simulated temporal changes in microtissue width. Simulated results are shown for $k_v = 1.5, 1.25, 1.0$. Experimental results are shown in red as mean ± SEM.

Fig. S4. Distribution and alignment of sarcomeres in the biaxial tissue at a number of time-points following signal initiation. at time t/θ=0: (a) t/θ=0.8; (b) t/θ=1.4; (c) t/θ=1.9; (d) t/θ=2.5; (e) t/θ=3.1; (f) t/θ=4.2; (g) t/θ=5.9; (h) t/θ=10.0. The quantity $\Pi = (\eta_{max} - \bar{\eta})$ is indicated by the vector color and vector length. The vector orientation indicates the orientation of η_{max}, (the direction of the dominant sarcomere formation) at all points in the tissue. The solid white outline in the top plot indicates the initial non-deformed tissue geometry.

Fig. S5. Distribution of the non-dimensional effective stress $\hat{S}$ in the biaxial tissue at a number of time-points following signal initiation at time t/θ=0: (a) t/θ=0.8; (b) t/θ=1.4; (c) t/θ=1.9; (d) t/θ=2.5; (e) t/θ=3.1; (f) t/θ=4.2; (g) t/θ=5.9; (h) t/θ=10.0. $\hat{S} = (\sigma^p_{max} - \sigma^p_{min})/\sigma^p_{max}$, where σ^p_{max} and σ^p_{min} are the maximum and minimum principal stresses, respectively. The magnitude of $\hat{S}$ is indicated by the vector color and vector length. The vector orientation indicates the maximum principal direction, i.e. the orientation of σ^p_{max}. The solid white outline in the top plot indicates the initial non-deformed tissue geometry.

Fig. S6. Distribution and alignment of sarcomeres in the uniaxial tissue at a number of time-points following signal initiation at time t/θ=0: (a) t/θ=0.6; (b) t/θ=1.2; (c) t/θ=2.9; (d) t/θ=4.6; (e) t/θ=5.8; (f) t/θ=10.0. The quantity $\Pi = (\eta_{max} - \bar{\eta})$ is indicated by the vector color and vector length. The vector orientation indicates the orientation of η_{max}, (the direction of the dominant sarcomere formation) at all points in the tissue. The solid white outline in the top plot indicates the initial non-deformed tissue geometry.

Fig. S7. Distribution of the non-dimensional effective stress $\hat{S}$ in the biaxial tissue at a number of time-points following signal initiation at time t/θ=0: (a) t/θ=0.6; (b) t/θ=1.2; (c) t/θ=2.9; (d) t/θ=4.6; (e) t/θ=5.8; (f) t/θ=10.0. $\hat{S} = (\sigma^p_{max} - \sigma^p_{min})/\sigma^p_{max}$, where σ^p_{max} and σ^p_{min} are the maximum and minimum principal stresses, respectively. The magnitude of $\hat{S}$ is indicated by the vector color and vector length. The vector orientation indicates the maximum principal direction, i.e. the orientation of σ^p_{max}. The solid white outline in the top plot indicates the initial non-deformed tissue geometry.

Fig. S8. Designs of microfabricated platforms for generating, cultivating, and assaying microtissues. (A, B) Substrate dimensions for microtissue seeding platforms. Uniaxial tension force microtissues which we termed cardiac microwire (CMW) exhibit increased cell elongation and cell alignment compared to biaxial tension force microtissues (BITF). (C, D) A 24-well cardiac bioreactor platform composed of platinum wire electrodes embedded in a microfabricated substrate is used to contain CMW from the point of seeding to cultivation to assaying.

Fig. S9. In-vivo-like aligned morphology of cardiomyocytes and non-cardiomyocytes can be recapitulated in vitro using aligned ECM-patterned substrates. (A) AFM micrographs of collagen deposited glass slides of various nanoscale architectures. (B) On glass, unaligned collagen, and aligned collagen substrates, heart cells show significantly diverse levels of density due to proliferation over 7 days. Bi-directional white arrow set indicate orientation of collagen alignment on substrates. Immunofluorescence shows Phalloidin-stained actin filaments (red), Cardiac TroponinT (green) and DAPI-stained nuclei (blue). Cell cytoskeleton alignment and striations (small white arrowheads) are observed in CM on aligned collagen.

Fig. S10. Immunofluorescence micrographs of non-dissociated hESC-CM aggregates (A), aggregates of 'B' condition (B), and CMW of 'B' condition (C). White arrows indicate the presence of putative FB stained with Vimentin in red.

Fig. S11. Histological sections and trichrome staining of aggregates of 'B' condition (A), and CMW of 'B' condition (B). Collagen is shown in blue, cytoplasm in pink, and nuclei in dark purple.

Fig. S12. Transmission electron microscopy images of aggregates of 'B' condition (A), and CMW of 'B' condition (B). Sarcomeres are indicated by red lines, Z-disks are indicated by black arrows, and H-zones are indicated by white arrows.

Table S1. Summary of CMW on day 7 (post-seeding) generated from mixing experiments indicating presence of: ECM remodeling, spontaneous contractions, synchronous contractions, tissue integrity, and amenability to electrophysiological (EP) measurements.

Table S2. Frequency of events of spontaneous CMW impulse propagation direction on day 7 (post-seeding). Normal rhythms were observed in CMW. Electrical stimulation was used to successfully reverse direction of impulse propagation. Data are reported as the mean ± SEM.

Table S3. Frequency of events of spontaneous CMW_{circ} impulse propagation on day 14 and day 21 (post-seeding). Both arrhythmia and normal rhythm were observed in CMW_{circ} at both time points. A 10V defibrillation on day 7 induced all CMW_{circ} to normal rhythm. Data are reported as the mean ± SEM.

Supplementary Table 1

	ECM remodeling	Spontaneous contractions	Synchronous contractions	Tissue integrity	EP measurement
CMW A	✓ (limited)	✓		✓	
CMW B	✓	✓	✓	✓	✓
CMW C	✓	✓ (limited)	✓		
CMW D	✓				

Supplementary Table 2

Tissue geometry: CMW	Spontaneous activation on day 7 (frequency)	Activation on day 7 after point stim. from opposite end (freq.)
Normal rhythm (right to left)	0.5	0.5
Normal rhythm (left to right)	0.5	0.5

Supplementary Table 3

Tissue geometry: CMW_{circ}	Spontaneous activation on day 14 (frequency)	Spont. activation on day 14 after 10 V field stim. (freq.)	Spontaneous activation on day 21 (freq.)
Arrhythmia	0.82 ± 0.08	0	0.05 ± 0.04
Normal rhythm	0.18 ± 0.08	1	0.95 ± 0.04

Supplementary Figure 1

Pattern Photoresist on glass substrate

Generate PDMS mold

Quick-cure angled droplet (3 µL) of PDMS on each post

Generate negative Polyurethane master

Replicate substrates with PDMS

Embed platinum wire electrodes for point stimulation

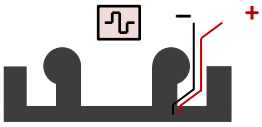

Outfit 24-well tissue culture plate with substrates

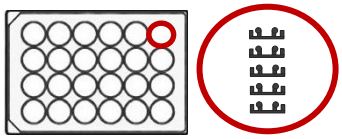

Add collagen mastermix and centrifuge at 300 g

Mix in cell-laden collagen

Centrifuge cell-laden collagen into recessions at 200 g

Aspirate excess cell-laden collagen and polymerize at 37 °C

Add cell culture media after 15 min.

Supplementary Figure 2

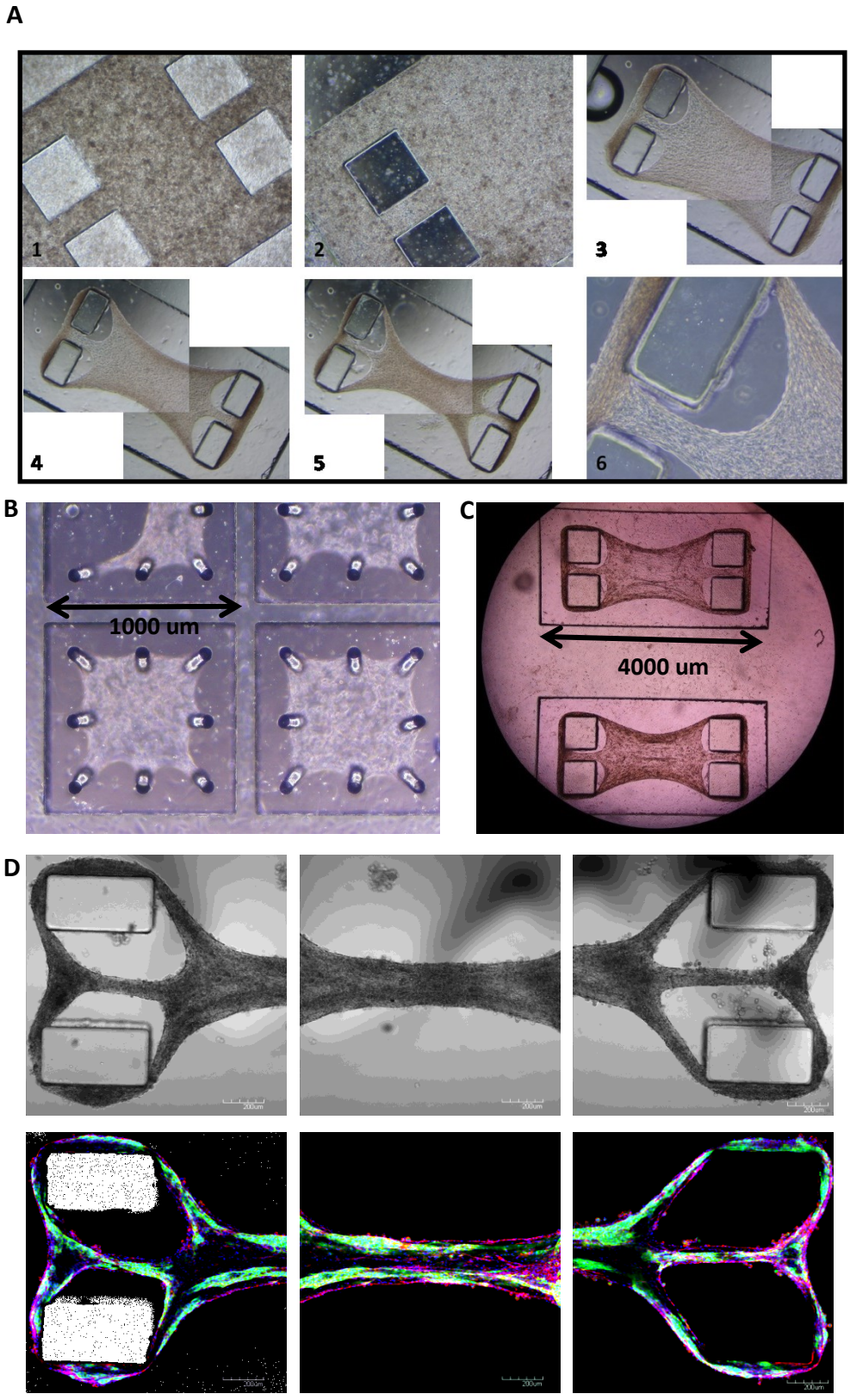

Supplementary Figure 3

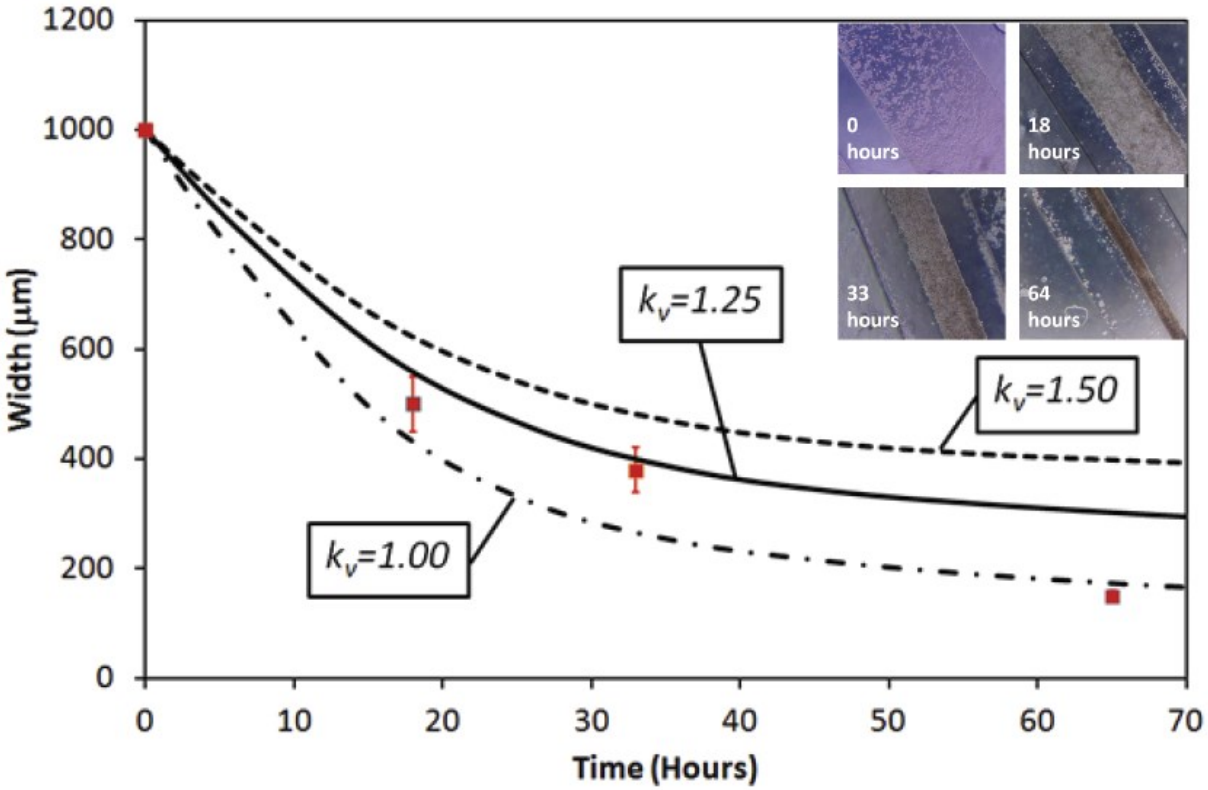

Supplementary Figure 4

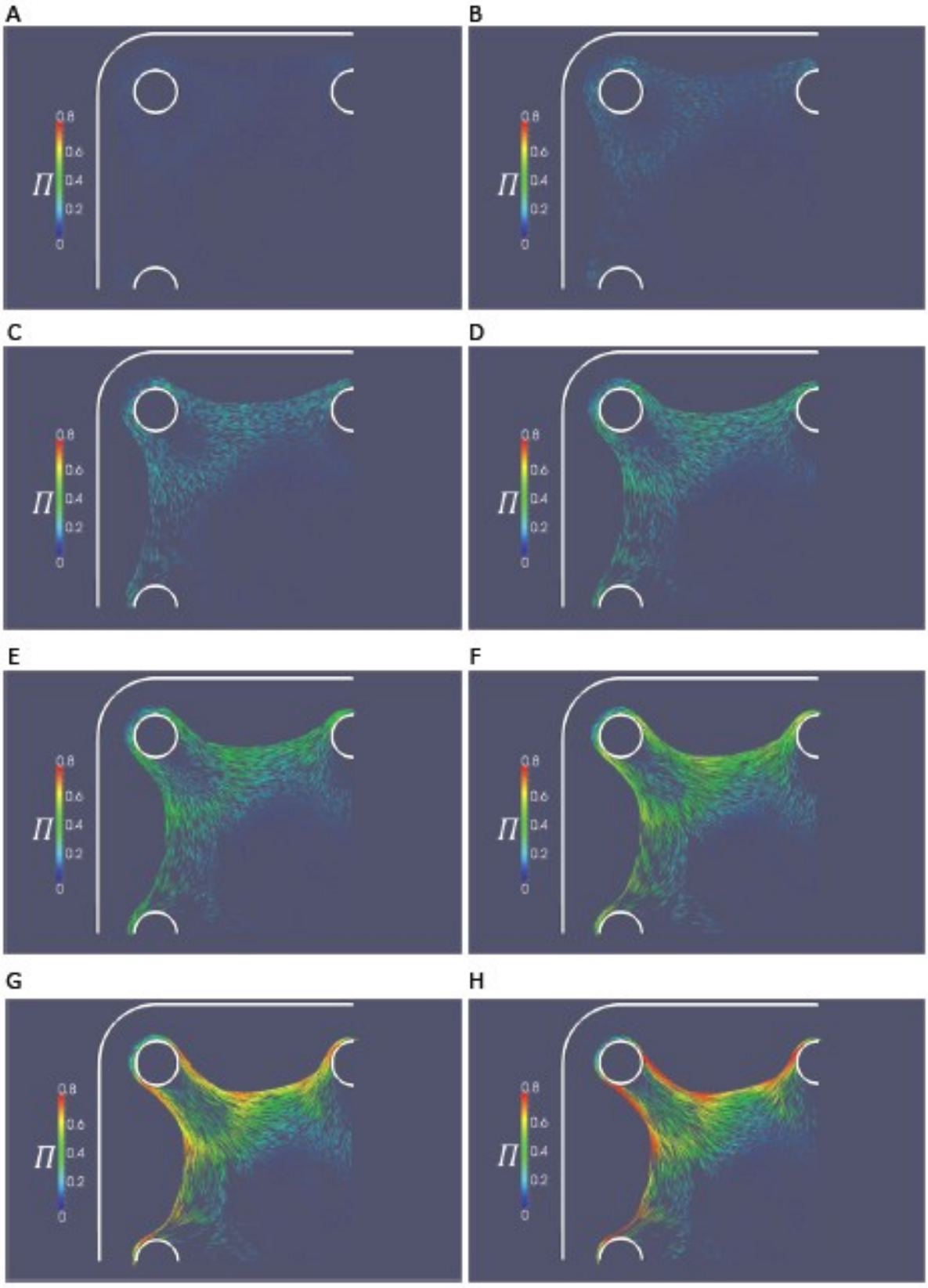

Supplementary Figure 5

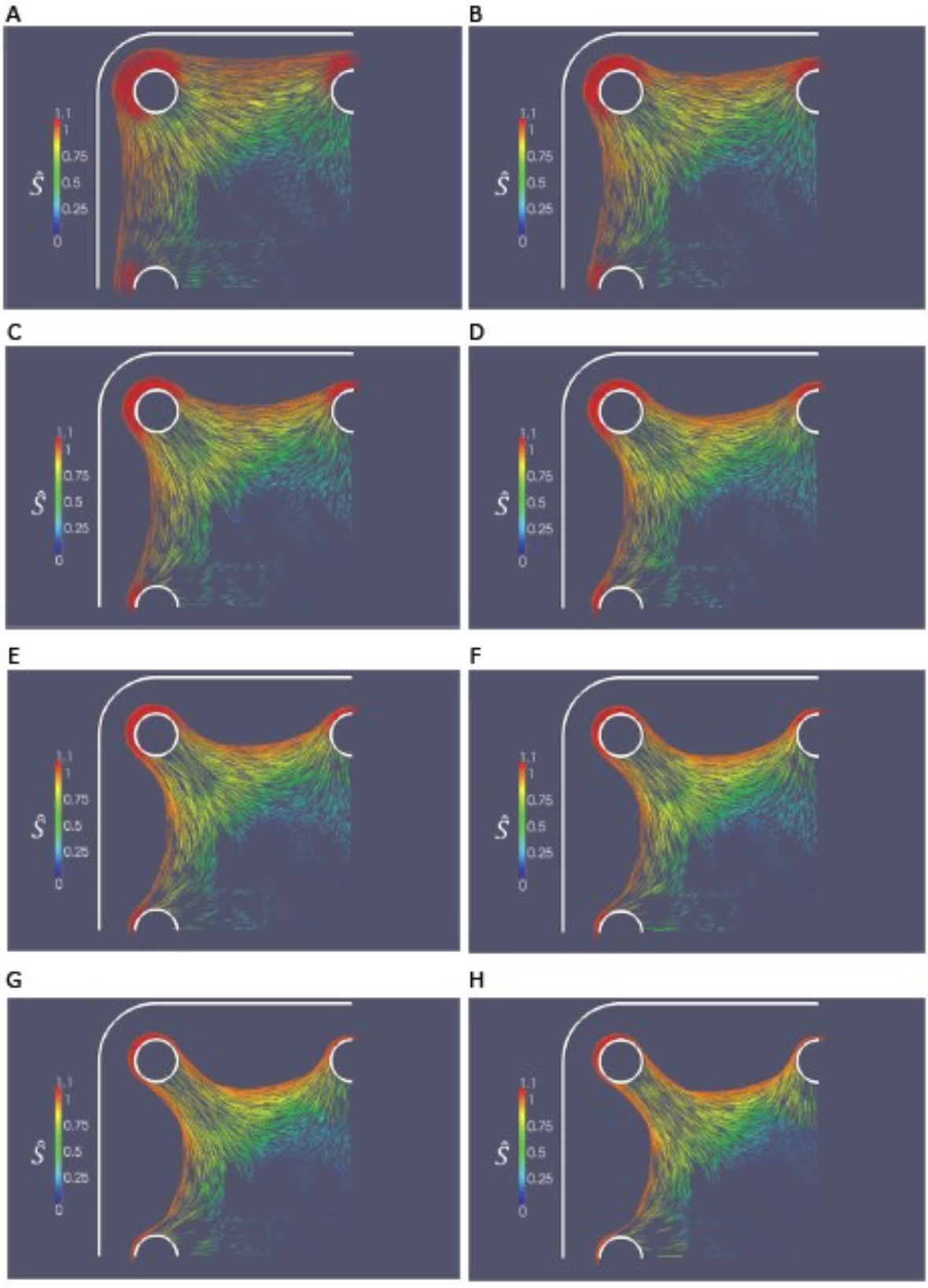

Supplementary Figure 6

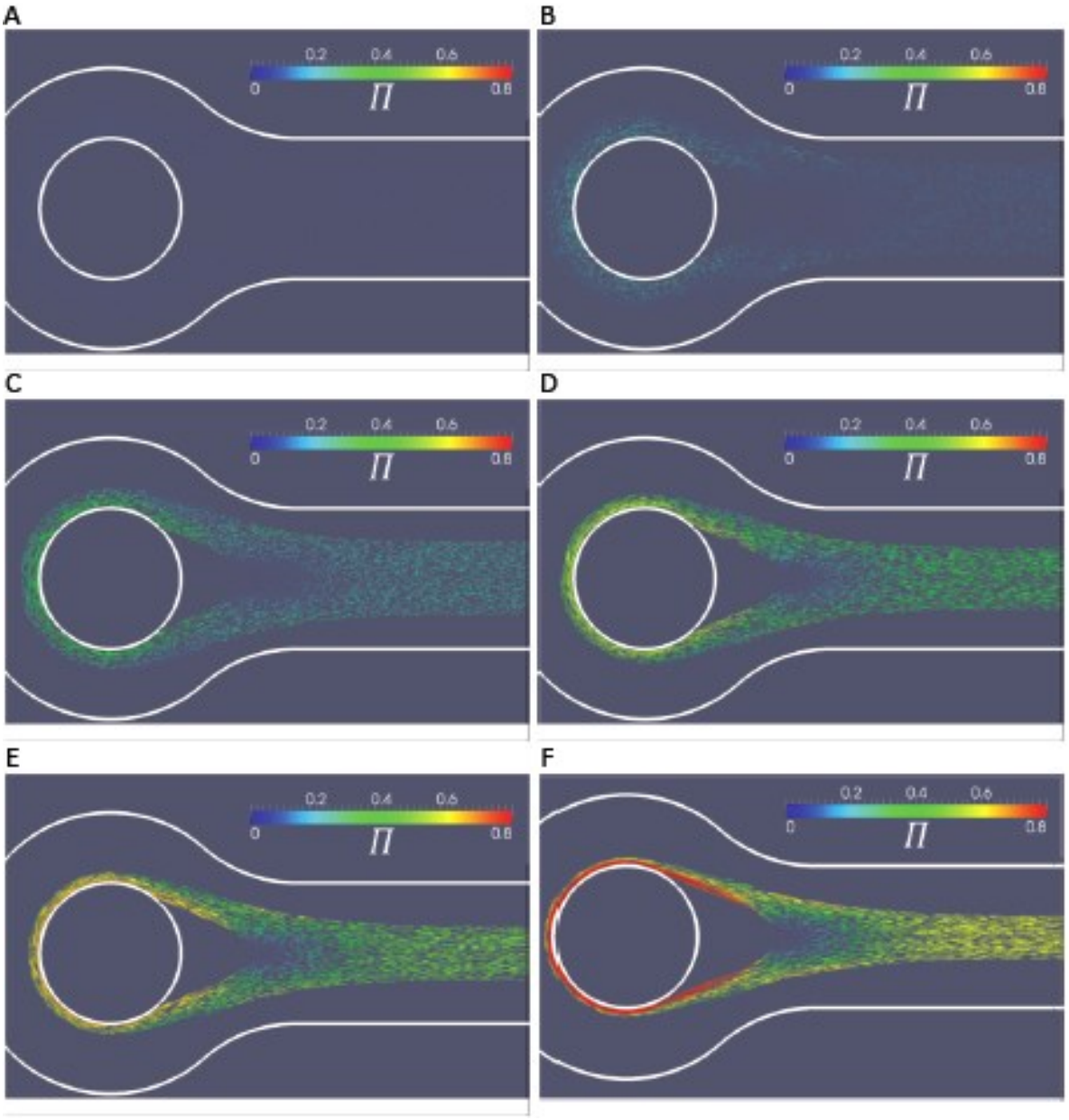

Supplementary Figure 7

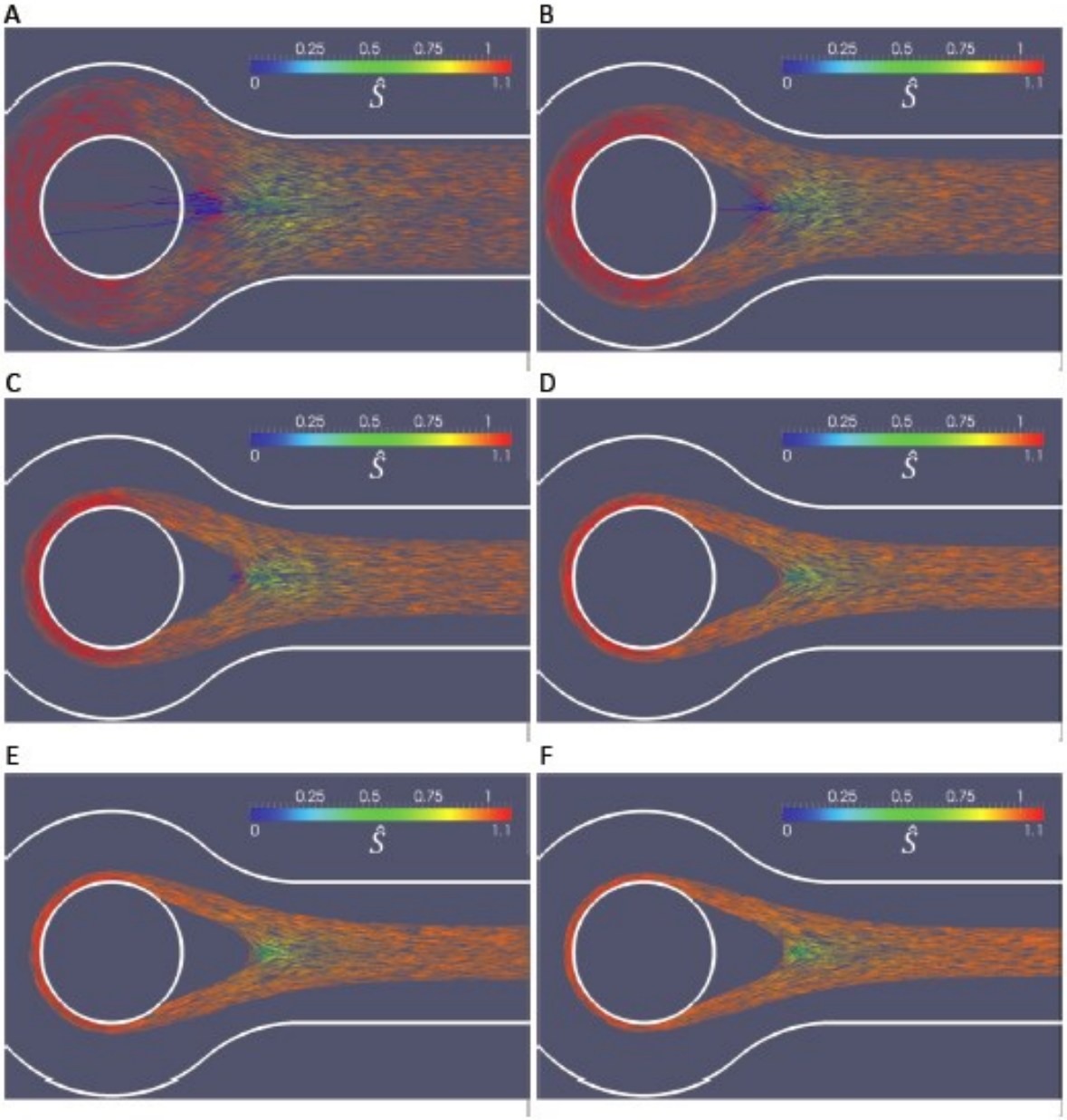

Supplementary Figure 8

A

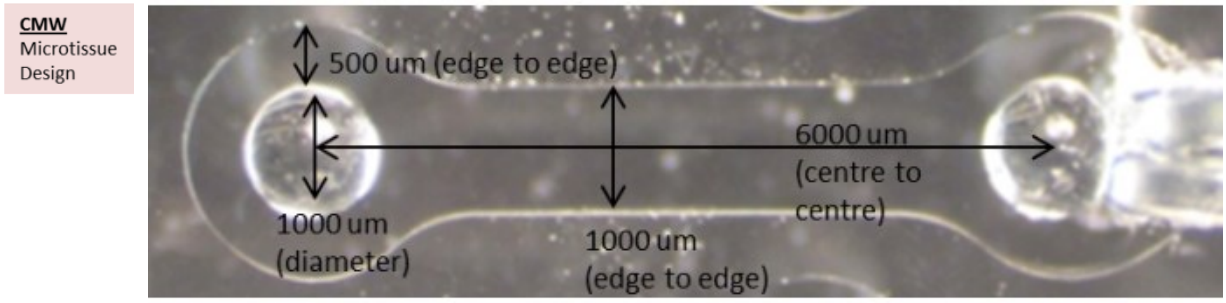

B

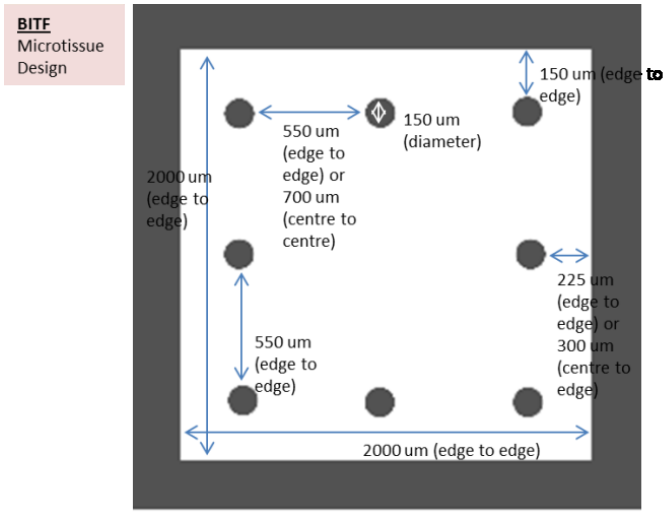

C

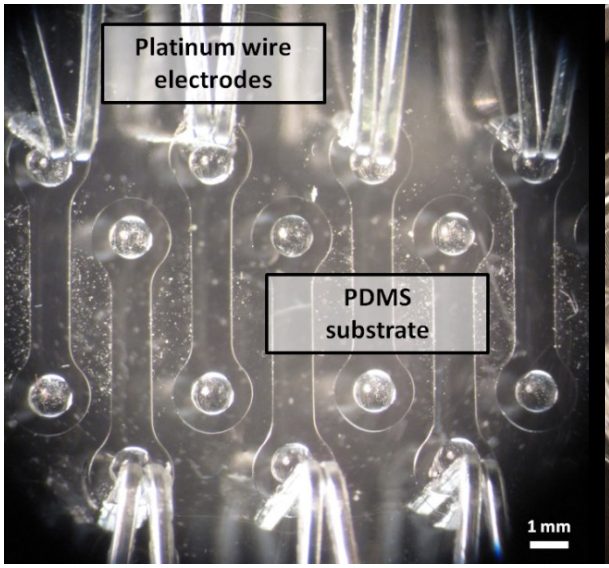

D

Supplementary Figure 9

A

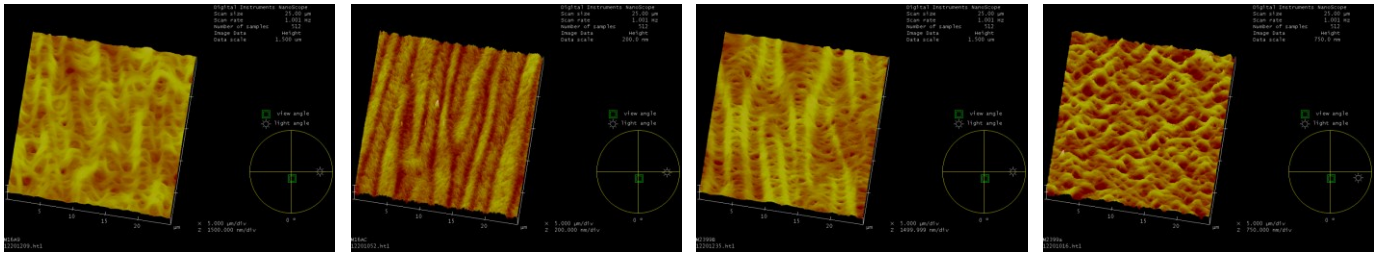

B

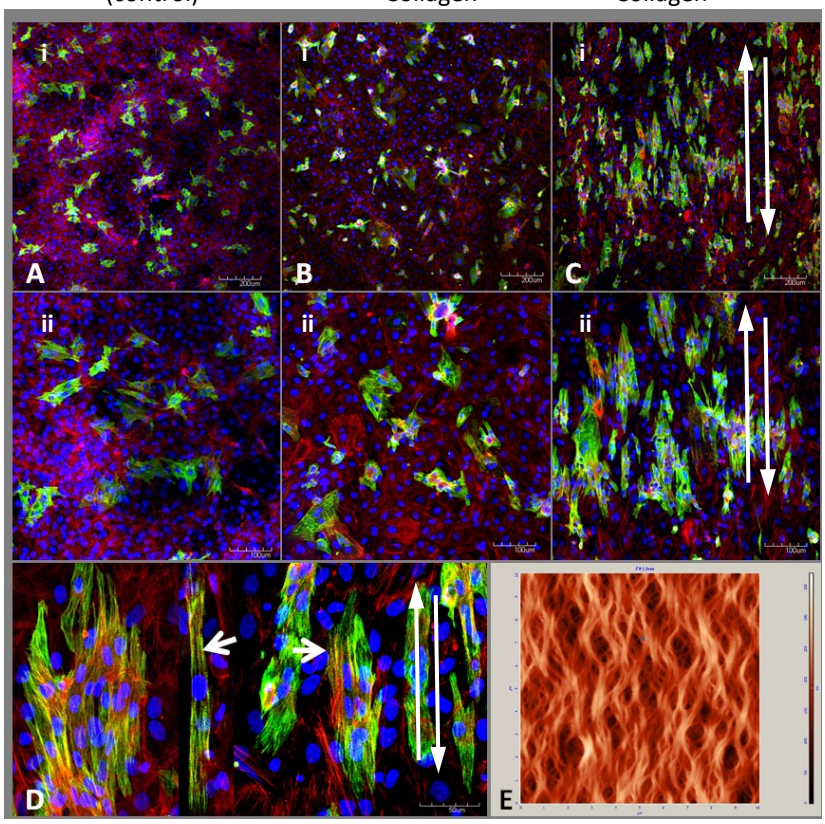

Supplementary Figure 10

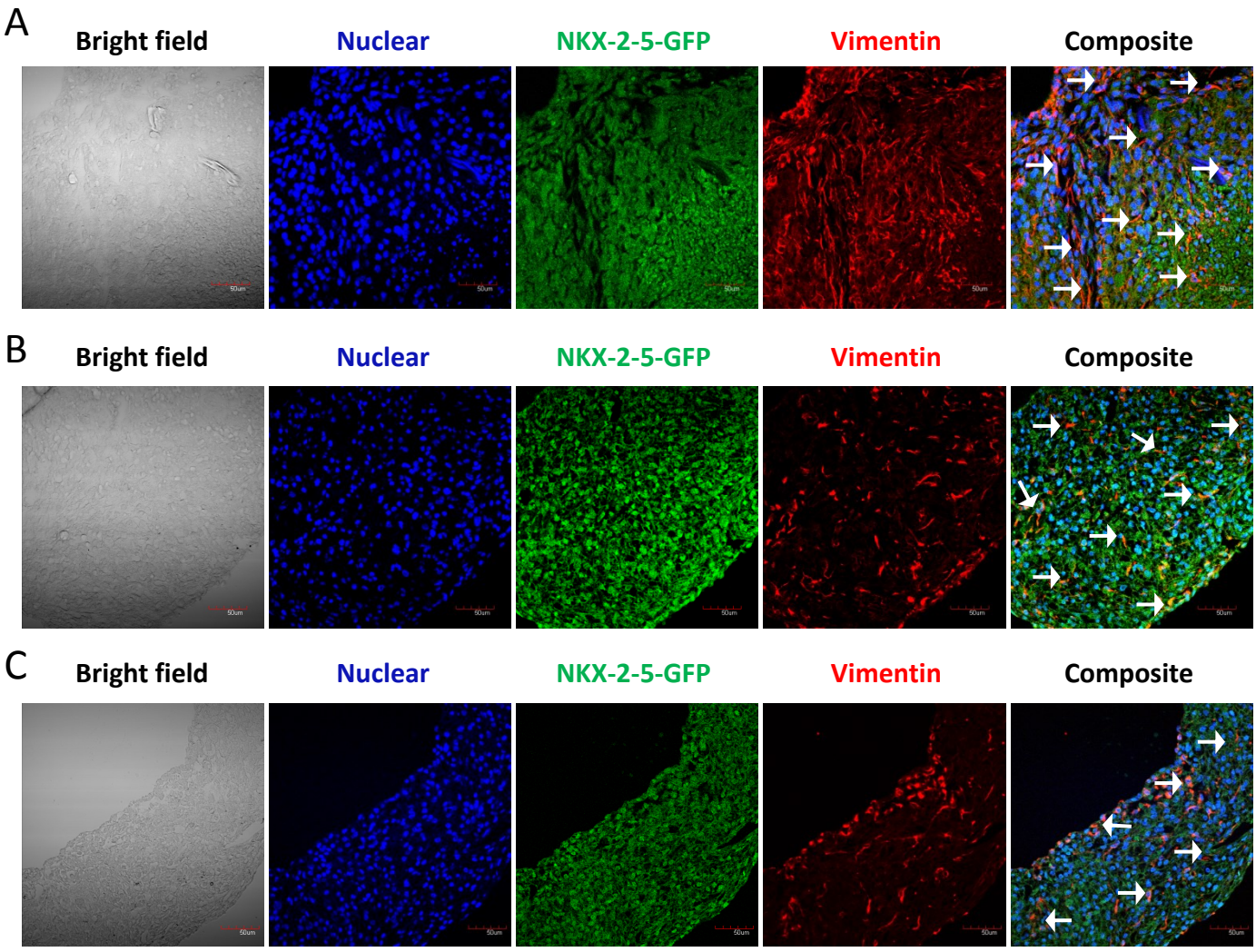

Supplementary Figure 11

A

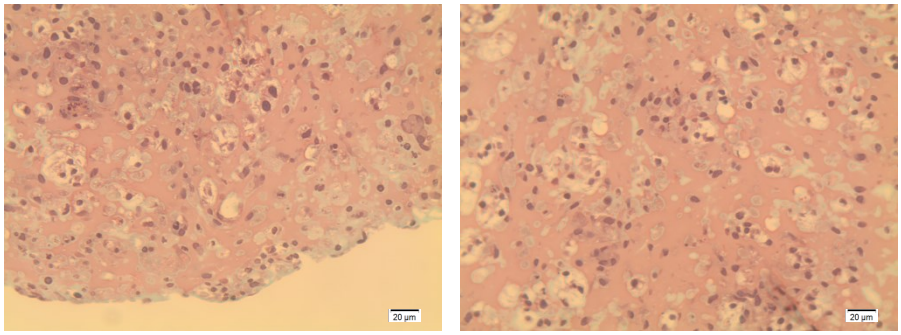

B

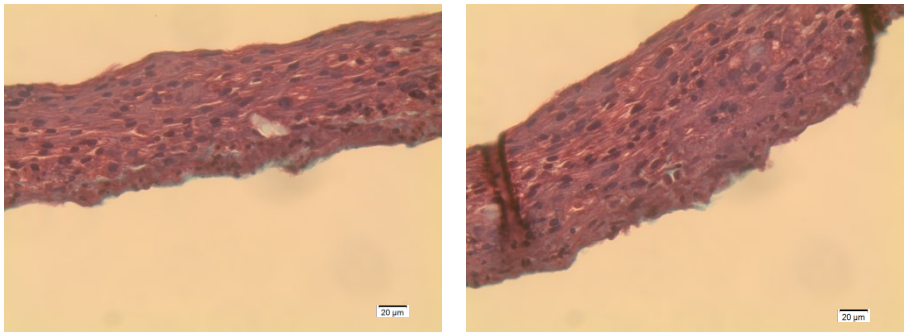

Supplementary Figure 12

A

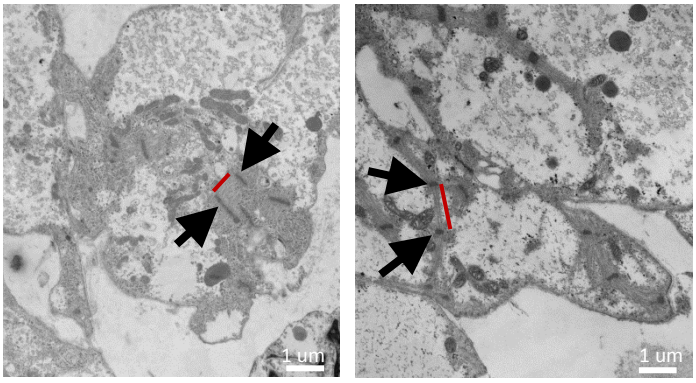

B

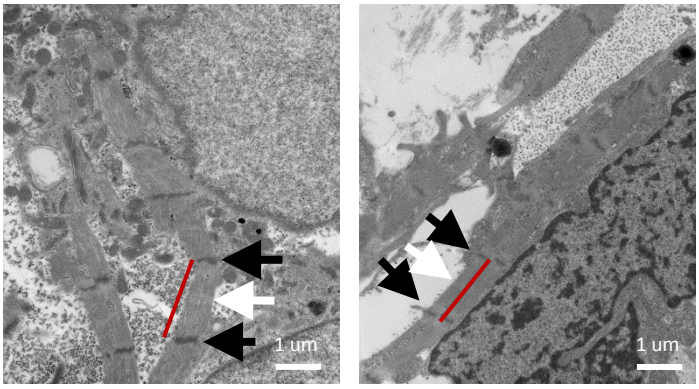

Appendix A: Computational methodology

The evolution and contractility of sarcomeric filaments in the microtissues is simulated using a previously proposed framework [1]. While this framework has previously been implemented for the modeling of stress fibers contractility in a range of cell phenotypes [2-5], here it is adapted for the simulation of sarcomeric filaments in cardiomyocytes on the basis that both stress fibers and sarcomeric filaments are composed of and operate via actin-myosin interactions. A full description of the governing equations is given below.

In this model, we make the following key assumptions: (i) there is sufficient actin and myosin in the cell such that the activation of the sarcomeric filaments in each direction is not limited by their availability, (ii) a representative volume element can be defined - specifically, a fine scale network of filaments exists on a length scale much smaller than the dimensions of the cell, and (iii) sarcomeric filaments can form in any direction/orientation with equal probability.

Mathematical formulation

Sarcomere formation is assumed to be driven by an exponentially decaying signal, where the signal intensity, C, in the tissue is given as

$$C = e^{\left(\frac{-t}{\theta}\right)} \tag{A1}$$

The signal may be thought of as the concentration of calcium or Rho. θ is a constant that controls the decay rate of the signal and t is the time elapsed since the signal initiation. The non-dimensional sarcomere activation level, $\eta(\phi)$, is computed in all directions (ϕ). A first order kinetic equation governs the evolution of sarcomeric filaments, whereby filament formation is driven by a signal (Rho GTPases) that decays exponentially with time via C as given by (A1) and a second term that captures the dissociation:

$$\dot{\eta}(\phi) = [1 - \eta(\phi)]\frac{Ck_f}{\theta} - \left(1 - \frac{\sigma(\phi)}{\sigma_0(\phi)}\right)\eta(\phi)\frac{k_b}{\theta} \tag{A2}$$

The dimensionless constants k_f and k_b govern the rates of formation and dissociation, respectively, of the filaments. Sarcomere contractility is modeled using a Hill-type equation, whereby the tension generated by a sarcomeric filament decreases with increasing shortening velocity. This is similar to that of skeletal muscle (both skeletal muscle and cardiomyocyte sarcomeric filaments produce tension due to actin-myosin interactions). The tension in a sarcomeric filaments, $\sigma(\phi)$, which is generated by cross-bridge cycling of actin-myosin pairs, is given as:

$$\frac{\sigma(\phi)}{\sigma_0(\phi)} = \begin{cases} 0 & \frac{\dot{\varepsilon}(\phi)}{\dot{\varepsilon_0}} \leq -\frac{\eta(\phi)}{k_v} \\ 1 + \frac{k_v}{\eta(\phi)}\frac{\dot{\varepsilon}(\phi)}{\dot{\varepsilon_0}} & -\frac{\eta(\phi)}{k_v} \leq \frac{\dot{\varepsilon}(\phi)}{\dot{\varepsilon_0}} \leq 0 \\ 1 & \frac{\dot{\varepsilon}(\phi)}{\dot{\varepsilon_0}} > 0 \end{cases} \tag{A3}$$

where $\sigma(\phi)$ is the sarcomere tension, $\sigma_0(\phi)$ is the isometric tension. The model parameter k_v determines the slope of the Hill curve, representing the reduction in stress upon increasing the shortening strain rate, $\dot{\varepsilon}(\phi)$, by $\dot{\varepsilon_0}$. The isometric tension of the sarcomere depends on the activation level of the sarcomere, $\eta(\phi)$, whereby$\sigma_0(\phi) = \eta(\phi)\sigma_{max}$. The model parameter $\sigma_{max}$is the maximum tension in a fully activated sarcomere.

The simulations performed in the present study are fully predictive, with sarcomeric filaments being allowed to form in all directions in the two-dimensional tissue. In equation A3 the axial strain rate $\dot{\varepsilon}(\phi)$ in the sarcomeric filament at angle ϕ is determined from the two dimensional strain rate tensor at each integration point such that

$$\dot{\varepsilon}(\phi) = \dot{\varepsilon}_{11}\mathrm{Cos}^2\phi + \dot{\varepsilon}_{22}\mathrm{Sin}^2\phi + \dot{\varepsilon}_{12}\mathrm{Sin}2\phi \qquad \text{(A4)}$$

The active sarcomeric contribution to the stress tensor at each integration point is given as

$$S_{ij}^{A} = \frac{1}{2\pi}\int_{-\pi/2}^{\pi/2}\begin{bmatrix} 2\sigma(\phi)\mathrm{Cos}^2\phi & \sigma(\phi)\mathrm{Sin}2\phi \\ \sigma(\phi)\mathrm{Sin}2\phi & 2\sigma(\phi)\mathrm{Sin}^2\phi \end{bmatrix} d\phi \qquad \text{(A5)}$$

The constitutive formulation is completed by the addition of a passive elastic contribution to represent the collagen matrix and the non-contractile components of cardiomyocytes. The passive stress is given as

$$S_{ij}^{P} = \frac{E}{1+\upsilon}\varepsilon_{ij} + \frac{E\upsilon}{(1-2\upsilon)(1+\upsilon)}\delta_{ij}\varepsilon_{kk} \qquad \text{(A6)}$$

Such that the total stress is given as

$$S_{ij} = S_{ij}^{A} + S_{ij}^{P} \qquad \text{(A7)}$$

This constitutive framework was implemented in ABAQUS (Dassault Systemes) as a user-defined material subroutine. Microtissue geometries were meshed using four noded plane stress elements (CPS4). Post-processing of results was performed using the software Paraview.

Finite element (FE) models are created for both the "biaxial" and "uniaxial" microtissue, as shown in Fig. 1. Undeformed FE geometries are based on initial microtissue geometries prior to deformation due to cardiomyocyte contractility and remodeling. The circular PDMS posts used to constrain the microtissues are modeled as rigid surfaces, as these supports are several orders stiffer than the surrounding microtissue. In the case of the biaxial FE model, the microtissue is assumed to be bonded to the eight supporting circular posts, reflecting the in-vitro coating of each post with an adhesive agent. In the case of the uniaxial microtissue such an adhesive agent was not used, hence in the uniaxial FE models hard contact is assumed between the two circular rigid posts and surrounding microtissue, allowing sliding and separation of the tissue from the posts. 4241 plane stress full integration elements were used for the uniaxial geometry while 37603 such elements were used for the biaxial geometry for all analyses following an initial mesh sensitivity study.

Model outputs

The formation of aligned contractile sarcomeres at each point in the tissue is predicted by the output parameter Π, defined as the difference between maximum and mean sarcomere activation level ($\Pi = \eta_{max} - \bar{\eta}$). Highly activated, aligned sarcomere formation in a dominant direction is predicted by a value of Π close to 1. In contrast, a value of Π close to 0 predicts that no dominant sarcomere has formed at that point. Predicted distributions of Π are directly comparable with fluorescent microscopy images stained for cardiac Troponin T and Alpha-Actinin, whereby removal of background fluorescence reveals the distribution of dominant sarcomere formation.

In order to investigate the relationship between sarcomere formation and the stress state of the tissue, a non-dimensional effective stress $\hat{S} = (\sigma_{max}^{p} - \sigma_{min}^{p})/\sigma_{max}^{p}$ is defined where σ_{max}^{p} and σ_{min}^{p} are the maximum and minimum principal stresses, respectively of the stress tensor S_{ij} defined in the mathematical formulation of the model,. If the stress state at a point in the tissue is perfectly bi-axial then $\sigma_{max}^{p} = \sigma_{min}^{p}$ so that $\hat{S} = 0$. On the other hand, if $\hat{S} = 1$ the stress state is perfectly uniaxial, with $\sigma_{min}^{p} = 0$.

Model calibration

Model parameters are calibrated based on experimentally observed changes in the width of the uniaxial tissue construct. As shown in Figure S3, a reasonable prediction of tissue deformation is obtained for a value of k_v between 1 and 1.5 with a ratio of $(\sigma_{max}/E) = 25$ and $\dot{\varepsilon}_o = 0.003s^{-1}$. This suggests that cardiomyocytes posess a higher value of isometric tension than NIH 3T3 cells considered in the study of Legant et al. [3] where $(\sigma_{max}/E) = 16$ for a microtissues constructed from 1.75 mg/ml collagen. Additionally, the low value of k_v (<1.5) calibrated for cardiomyocytes in the present study indicates that the slope of the Hill curve is low for this cell type tension in comparison to 3T3 cells ($k_v = 2$) (this indicates that cardiomyocytes will produce a tension closer to the isometric value than will 3T3 cells for a given shortening strain rate. A value of $k_v = 1.25$ is used for all subsequent simulations in the present study. The temporal behaviour of the tissue, with a steady state tissue width being observed following 70 hours, is arbitrarily captured by adjusting the decay time of the signal C and the reaction rate constants k_f and k_b in equation 1. For example, in Figure C2 a signal decay constant $\theta = 25200s$ (7 hours) is chosen, with $k_f/\theta = 0.14$ and $k_f/\theta = 0.014$.

Supplementary Model Results

Fig. 2B (bottom panel) shows a plot of the predicted sarcomere distribution in the uniaxial tissue following 70 hours (steady state). The tissue has deformed significantly from its initial geometry undergoing a significant reduction in width. Additionally, the tissue separates from the inner surface of the circular support due to the contractile action of the sarcomeres. A high degree of highly aligned sarcomere formation is computed throughout the central region of the tissue, with sarcomeres aligned along the major axis of the tissue. Additionally, a high degree of highly aligned sarcomere formation is computed in the narrow strips that form where the tissue separates from the supports. Low sarcomere formation is predicted in the localized "junction" region where these narrow strips meet. The predicted deformation of the tissue and the predicted distribution and alignment of sarcomeres correlates very closely with experimental observations. The evolution of tissue deformation and sarcomere formation is shown in Fig. S6 at a number of discrete time-points.

Fig. 2B (top panel) shows the stress state in the tissue, with vector directions indicating the direction of the maximum principal stress. The non-dimensional effective stress $\hat{\mathrm{S}} = (\sigma^{\mathrm{p}}_{\mathrm{max}} - \sigma^{\mathrm{p}}_{\mathrm{min}})/\sigma^{\mathrm{p}}_{\mathrm{max}}$ is close to 1 throughout the tissue, indicating that the stress state is highly uniaxial. A high degree of sarcomere formation is predicted in such regions of uniaxial stress (see Fig. 2B (bottom panel)). In contrast, $\hat{\mathrm{S}} \approx 0$ in the localised "junction" region where low sarcomere formation is predicted. It is worth noting that directions of maximum principal stress correlate strongly with the predicted directions of sarcomere formation throughout the tissue. The evolution of tissue deformation and non-dimensional effective stress $\hat{\mathrm{S}}$ is shown in Fig. S7 at a number of discrete time-points.

Fig. 2A (right panel) shows a plot of the predicted sarcomere distribution in the biaxial tissue following 70 hours (steady state). The tissue has deformed significantly from its initial geometry with significant curving of the of the tissue boundaries being observed. In this case, no separation of the tissue from the circular supports is permitted, as discussed above. The predicted tissue deformation corresponds closely with experimental observation. A high degree of aligned sarcomere formation is predicted in the peripheral regions of the tissue where sarcomeres are predicted to align parallel to the tissue boundaries. Additionally, moderate sarcomere formation is predicted near the four corner supports. Very little sarcomere formation is predicted in the centre of the tissue. The predicted deformation of the tissue and

the predicted distribution and alignment of sarcomeres correlates very closely with experimental observations. The evolution of tissue deformation and sarcomere formation is shown in Fig. S4 at a number of discrete time-points.

Fig. 2A (left panel) shows the stress state in the tissue, again with vector directions indicating the direction of the maximum principal stress. The non-dimensional effective stress $\hat{S}$ is close to 1 near the periphery of the tissue, indicating a uniaxial stress state. Again, this demonstrates a strong correlation between sarcomere formation and regions of uniaxial stress, with sarcomeres aligning in directions of maximum principal stress. In the centre of the tissue $\hat{S} \approx 0$, indicating a biaxial stress state. No sarcomere formation is predicted in this region of biaxial stress. The evolution of tissue deformation and non-dimensional effective stress $\hat{S}$ is shown in Fig. S5 at a number of discrete time-points.

Appendix B: Experimental methodology

Quantitative polymerase chain reaction primers

gene	forward	reverse
hNKX2-5	5'-TTTGCATTCACTCCTGCGGAGACCTA-3'	5'-ACTCATTGCACGCTGCATAATCGC-3'
hRYR2	5'-TGGGCCCAAGAATGACTTGGAAGA-3'	5'-TTGTCAACACGATCGGGCACTAGA-3'
hSERCA2	5'-ACATTGCTGCTGGGAAAGCTATGG-3'	5'-TTCTGTTGCCACCATTTCATCCCG-3'
hCX43	5'-GGCTTTTAGCGTGAGGAAAGTACCA-3'	5'-TCCCCAGCAGCAGGATTCGG-3'
hcTNT	5'-TTCACCAAAGATCTGCTCCTCGCT-3'	5'-TTATTACTGGTGTGGAGTGGGTGTGG-3'
hDDR2	5'-ACCAGCCATTTGTCCTGACTCTGT-3'	5'-ATCACTCGTCGCCTTGTTGAAGGA-3'
hSIRPA	5'-ACCTGGCTCAGGCTAGTTCCAAAT-3'	5'-TGTGCACACGTATGTGCTGTCTCT-3'
hBNP	5'-TTCCTGGGAGGTCGTTCCCAC-3'	5'-CATCTTCCTCCCAAAGCAGCC-3'
hANF	5'-GAACCAGAGGGGAGAGACAGAG-3'	5'-CCCTCAGCTTGCTTTTTAGGAG-3'
hMYL7	5'-ACATCATCACCCATGGAGACGAGA-3'	5'-GCAACAGAGTTTATTGAGGTGCCC-3'
hMYL2	5'-TGTCCCTACCTTGTCTGTTAGCCA-3'	5'-ATTGGAACATGGCCTCTGGATGGA-3'
hMYH6	5'-TCAGCTGGAGGCCAAAGTAAAGGA-3'	5'-TTCTTGAGCTCTGAGCACTCGTCT-3'
hMYH7	5'-TCGTGCCTGATGACAAACAGGAGT-3'	5'-ATACTCGGTCTCGGCAGTGACTTT-3'
hTBP	5'-TGAGTTGCTCATACCGTGCTGCTA-3'	5'-CCCTCAAACCAACTTGTCAACAGC-3'

REFERENCES

1. Deshpande V, McMeeking R, Evans A: **A bio-chemo-mechanical model for cell contractility**. *Proceedings of the National Academy of Sciences of the United States of America* 2006, **103**(38):14015-14020.
2. Deshpande VS, McMeeking RM, Evans AG: **A model for the contractility of the cytoskeleton including the effects of stress-fibre formation and dissociation**. *Proceedings of the Royal Society A: Mathematical, Physical and Engineering Science* 2007, **463**(2079):787-815.
3. Legant W, Pathak A, Yang M, Deshpande V, McMeeking R, Chen C: **Microfabricated tissue gauges to measure and manipulate forces from 3D microtissues**. *Proceedings of the National Academy of Sciences of the United States of America* 2009, **106**(25):10097-10102.
4. McGarry J, Fu J, Yang M, Chen C, McMeeking R, Evans A, Deshpande V: **Simulation of the contractile response of cells on an array of micro-posts**. *Philosophical transactions Series A, Mathematical, physical, and engineering sciences* 2009, **367**(1902):3477-3497.
5. Pathak A, Deshpande V, McMeeking R, Evans A: **The simulation of stress fibre and focal adhesion development in cells on patterned substrates**. *Journal of the Royal Society, Interface / the Royal Society* 2008, **5**(22):507-524.
6. Dowling E, Ronan W, Ofek G, Deshpande V, McMeeking R, Athanasiou K, McGarry J: **The effect of remodelling and contractility of the actin cytoskeleton on the shear resistance of single cells: a computational and experimental investigation**. *Journal of the Royal Society, Interface / the Royal Society* 2012, **9**(77):3469-3479.
7. Dowling E, Ronan W, McGarry J: **Computational investigation of in situ chondrocyte deformation and actin cytoskeleton remodelling under physiological loading**. *Acta biomaterialia* 2013, **9**(4):5943-5955.
8. Ronan W, Deshpande V, McMeeking R, McGarry J: **Numerical investigation of the active role of the actin cytoskeleton in the compression resistance of cells**. *Journal of the mechanical behavior of biomedical materials* 2012, **14C**:143-157.

Supporting Information

Thavandiran et al. 10.1073/pnas.1311120110

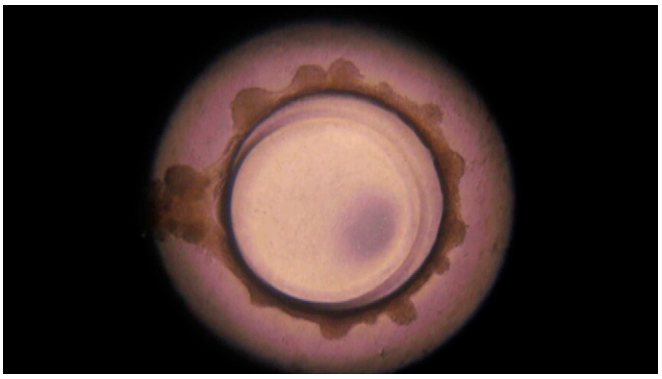

Movie S1. Distal component of cardiac microwire (CMW) A (100% NKX2-5+, 0% CD90+).

Movie S1

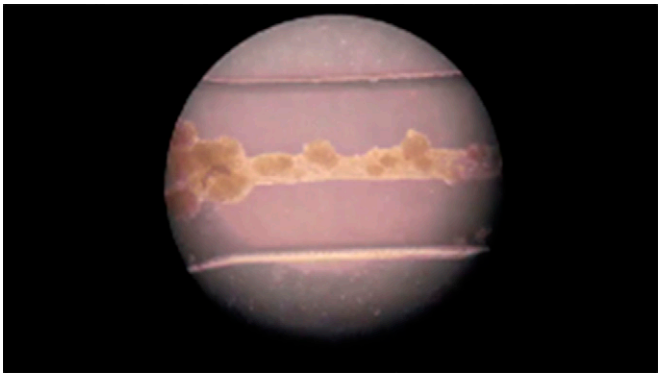

Movie S2. Medial component of CMW A (100% NKX2-5+, 0% CD90+).

Movie S2

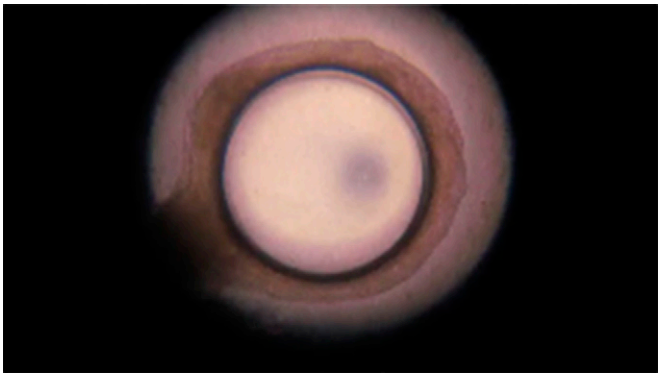

Movie S3. Distal component of CMW B (75% NKX2-5+, 25% CD90+).

Movie S3

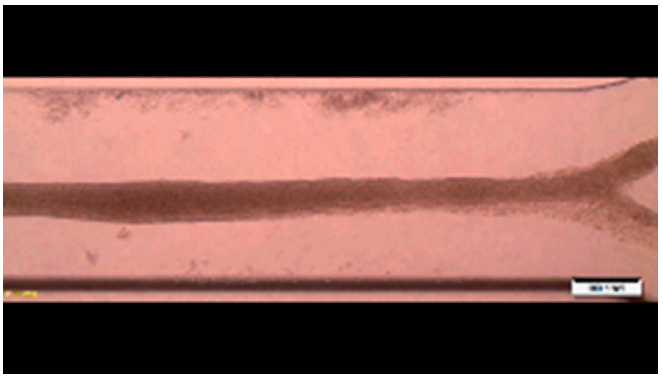

Movie S4. Medial component of CMW B (75% NKX2-5+, 25% CD90+).

Movie S4

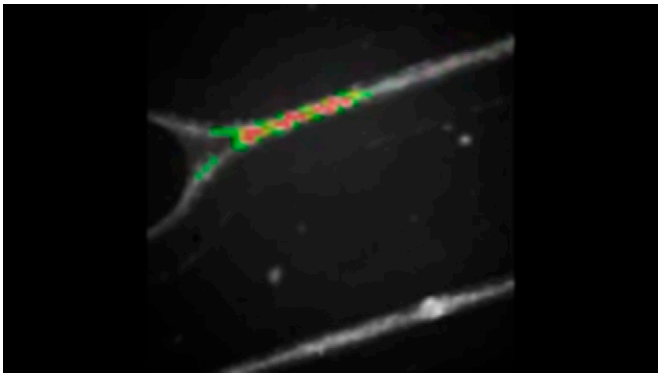

Movie S5. Impulse propagation of CMWs in normal rhythm (traversing right to left).

Movie S5

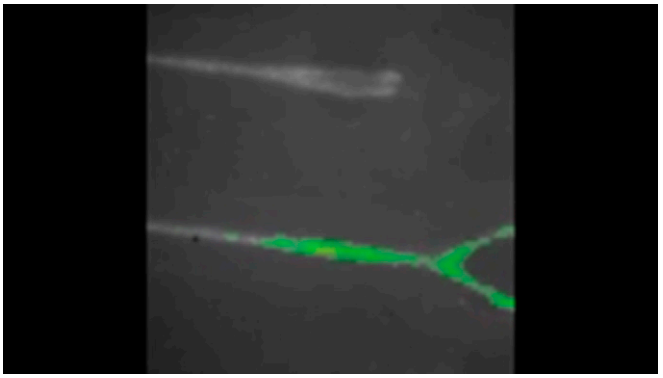

Movie S6. Impulse propagation of CMWs in normal rhythm (traversing left to right before reversal of direction using electrical stimulation).

Movie S6

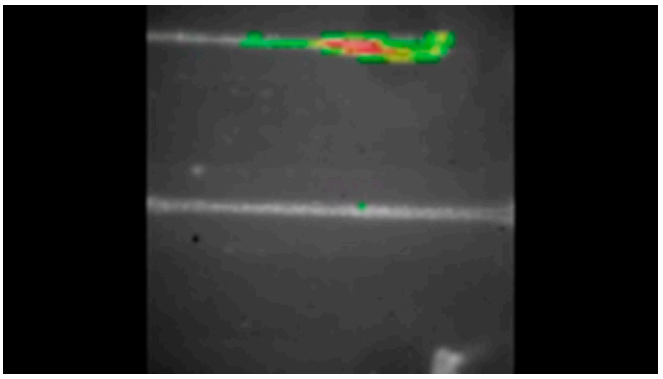

Movie S7. Impulse propagation of CMWs in normal rhythm (now traversing right to left after point electrical stimulation from the right distal end of the CMWs to reverse direction).

Movie S7

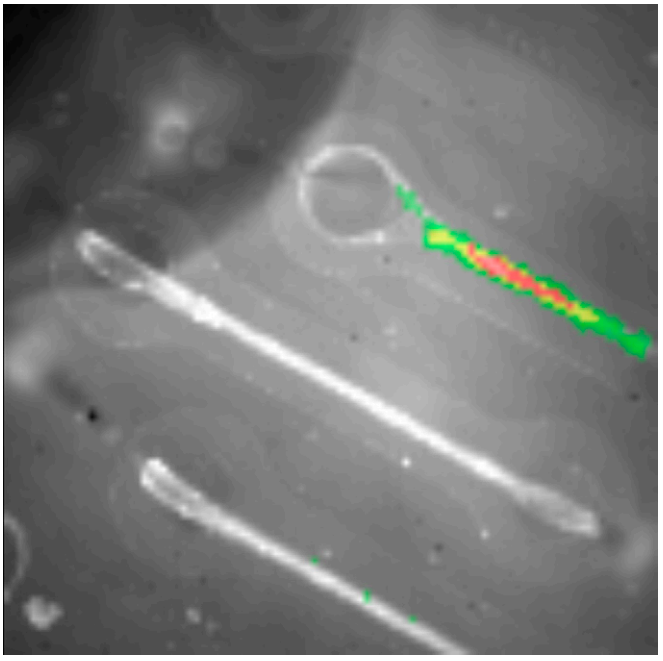

Movie S8. Impulse propagation of CMWs (at the medial–distal junction) obstructed by a conduction block, resulting in an incomplete reentrant wave-like system.

Movie S8

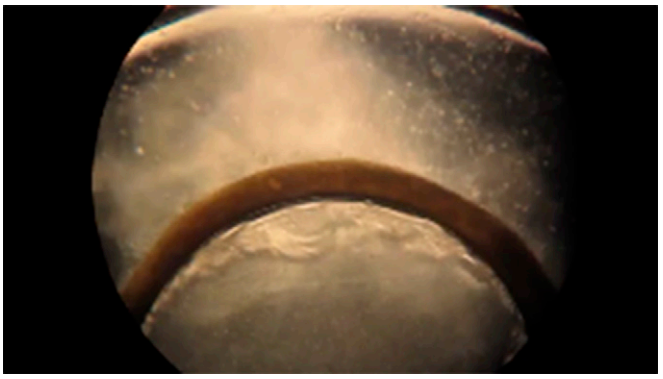

Movie S9. Circular CMWs (CMW_{circ}) on day 14 (postseeding), single well.

Movie S9

Movie S10. CMW_{circ} on day 14 (postseeding), reproducibility of multiple wells.

Movie S10

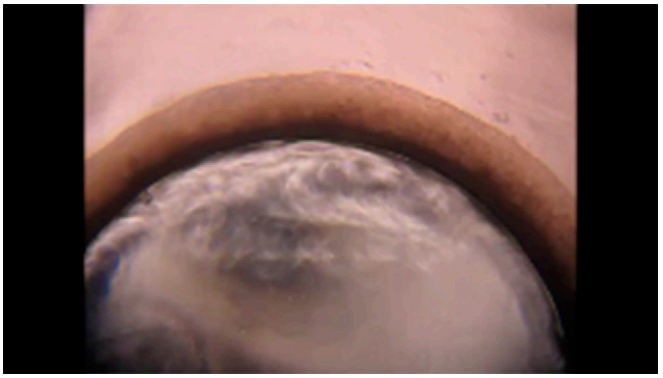

Movie S11. CMW_{circ} on day 14 (postseeding), in arrhythmia.

Movie S11

Movie S12. CMW_{circ} on day 14 (postseeding), in normal rhythm.

Movie S12

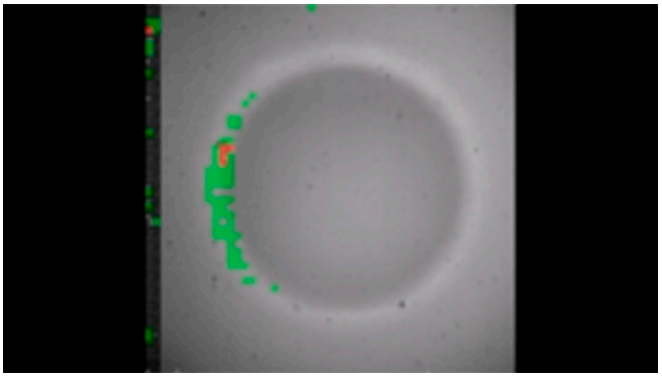

Movie S13. Impulse propagation of CMW_{circ} on day 14 (postseeding) in arrhythmia.

Movie S13

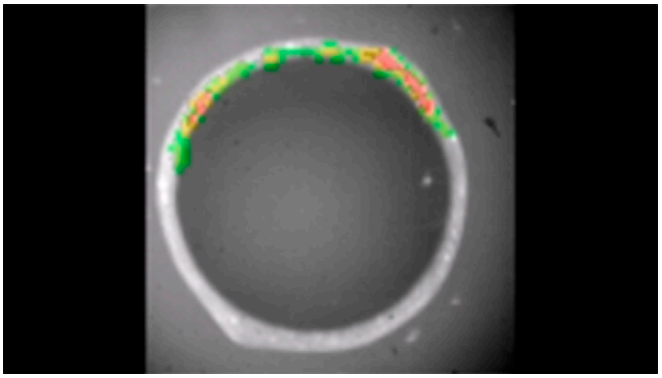

Movie S14. Impulse propagation of CMW_{circ} on day 14 (postseeding) in normal rhythm.

Movie S14